Cell Reports

Article

Targeting the USP7/RRM2 axis drives senescence and sensitizes melanoma cells to HDAC/LSD1 inhibitors

Graphical abstract

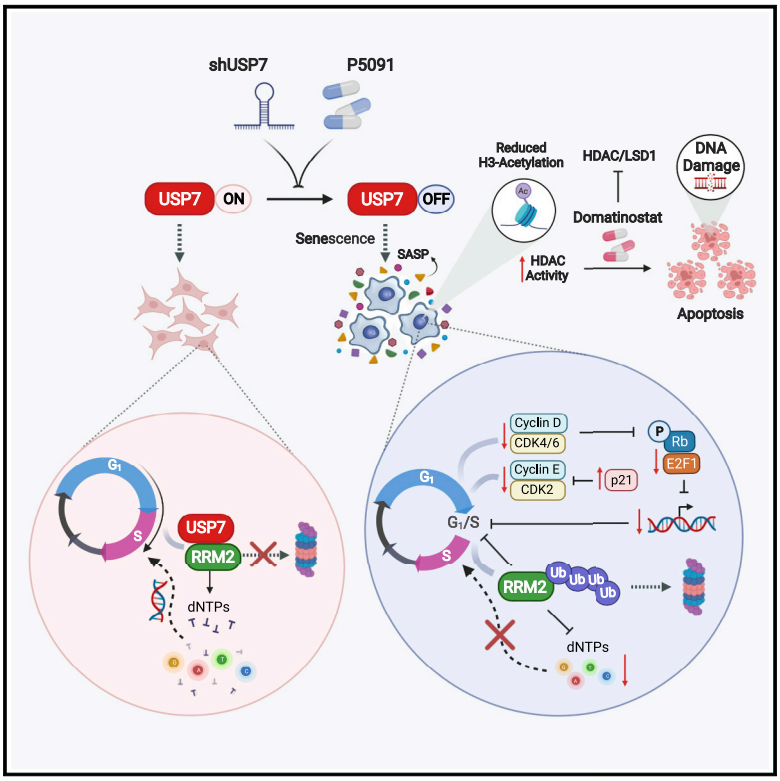

Highlights

- Genetic and pharmacological inhibition of USP7 induces senescence in melanoma PDXs
- USP7 stabilizes RRM2 by deubiquitination, protecting it from proteasome degradation
- Ectopic expression of RRM2 rescues shUSP7-induced senescent phenotype
- The HDAC/LSD1 inhibitor domatinostat clears senescent cells induced by USP7 inhibition

Authors

Letizia Granieri, Federica Marocchi, Marine Melixetian, ..., Giovanni Bertalot, Daniela Bossi, Luisa Lanfrancone

Correspondence

luisa.lanfrancone@ieo.it

In brief

Granieri et al. describe the prognostic role of USP7 in melanoma and provide evidence of the direct functional interaction of USP7 and RRM2. The USP7/RRM2 axis regulates cell cycle progression and, in turn, senescence. The work proposes a combination therapy for individuals with melanoma by combining USP7 and HDAC/LSD1 inhibitors.

Granieri et al., 2022, Cell Reports *40*, 111396
September 20, 2022
https://doi.org/10.1016/j.celrep.2022.111396

CellPress

Cell Reports

CellPress
OPEN ACCESS

Article

Targeting the USP7/RRM2 axis drives senescence and sensitizes melanoma cells to HDAC/LSD1 inhibitors

Letizia Granieri,[1] Federica Marocchi,[1] Marine Melixetian,[1] Neda Mohammadi,[1,2] Paola Nicoli,[1] Alessandro Cuomo,[1] Tiziana Bonaldi,[1] Stefano Confalonieri,[1] Federica Pisati,[3] Giuseppina Giardina,[1] Giovanni Bertalot,[1,4] Daniela Bossi,[1,5] and Luisa Lanfrancone[1,6,*]

[1]Department of Experimental Oncology, IEO, European Institute of Oncology IRCCS, 20139 Milan, Italy
[2]Experimental Hematology Unit, Division of Immunology, Transplantation, and Infectious Diseases, IRCCS San Raffaele Scientific Institute, 20132 Milan, Italy
[3]Histopathology Unit, Cogentech S.C.a.R.L, Via Adamello, 20139 Milan, Italy
[4]U.O.M. Anatomia ed Istologia Patologica, Ospedale S. Chiara di Trento, Largo Medaglie d'Oro, 38122 Trento, Italy
[5]Institute of Oncology Research, Oncology Institute of Southern Switzerland, Bellinzona, Switzerland
[6]Lead contact
*Correspondence: luisa.lanfrancone@ieo.it
https://doi.org/10.1016/j.celrep.2022.111396

SUMMARY

Deubiquitinating enzymes are key regulators of the ubiquitin-proteasome system and cell cycle, and their dysfunction leads to tumorigenesis. Our *in vivo* drop-out screens in patient-derived xenograft models identify USP7 as a regulator of melanoma. We show that USP7 downregulation induces cellular senescence, arresting melanoma growth *in vivo* and proliferation *in vitro* in BRAF- and NRAS-mutant melanoma. We provide a comprehensive understanding of targets and networks affected by USP7 depletion by performing a global transcriptomic and proteomics analysis. We show that RRM2 is a USP7 target and is regulated by USP7 during S phase of the cell cycle. Ectopic expression of RRM2 in USP7-depleted cells rescues the senescent phenotype. Pharmacological inhibition of USP7 by P5091 phenocopies the shUSP7-induced senescent phenotype. We show that the bifunctional histone deacetylase (HDAC)/LSD1 inhibitor domatinostat has an additive antitumor effect, eliminating P5091-induced senescent cells, paving the way to a therapeutic combination for individuals with melanoma.

INTRODUCTION

A fundamental trait of melanoma is cell cycle dysregulation leading to uncontrolled proliferation (Hanahan and Weinberg, 2011). A high mitosis rate is associated with aggressive histological features (Shen et al., 2014), and targeting cell cycle regulators has been proposed as a promising strategy in melanoma therapy (Xu and Mcarthur, 2016). Cell cycle progression is tightly controlled by the ubiquitin-proteasome system (UPS) (Nakayama and Nakayama, 2006). Ubiquitination is a reversible process, counterbalanced by the activity of ~100 deubiquitinases (DUBs) (Li and Reverter, 2021). In melanoma, on one hand, DUBs promote proliferation (Zhao et al., 2011) and drug resistance (Wei et al., 2021), and on the other hand, they enhance cisplatin's anticancer effect (Guo et al., 2020). USP7, one of the most studied DUBs in cancer, has oncogenic and tumor suppressor functions by regulating many different substrates (Bhattacharya et al., 2018). USP7 loss induces cell cycle arrest in G1 (Yi et al., 2016; Giovinazzi et al., 2013) or G2/M phase, leading to apoptosis (Peng et al., 2019). Despite being a promising target, with specific therapeutic inhibitors tested in several cancer types (Chen et al., 2021), its function is poorly elucidated in melanoma.

By carrying out an *in vivo* drop-out screen in patient-derived xenograft (PDX) models, we demonstrate that USP7 sustains the proliferation of BRAF- and NRAS-mutant melanomas. We extensively investigated the oncogenic role of USP7, underscoring its function in tumor growth and cell cycle progression. We report for the first time that USP7 loss induces a senescent phenotype in melanoma regardless of the harbored mutation. We found that RRM2 (ribonucleotide reductase subunit M2) is a novel binding partner and functional target of USP7. RRM2 is a cell cycle -regulated, rate-limiting enzyme that ensures that deoxyribonucleotides synthesis progresses through G1-S phase (Nordlund and Reichard, 2006; Chabes et al., 2004; Degregori et al., 1995). RRM2 loss induces cell cycle arrest and senescence in melanoma (Fatkhutdinov et al., 2016). It is mainly expressed during S phase, and its expression is regulated at the transcriptional level by E2F or at the post-translational level (Chabes et al., 2004; Degregori et al., 1995), as also shown in our PDX models. Its turnover is mainly determined by ubiquitin ligases complexes (Chabes et al., 2003; D'angiolella et al.,

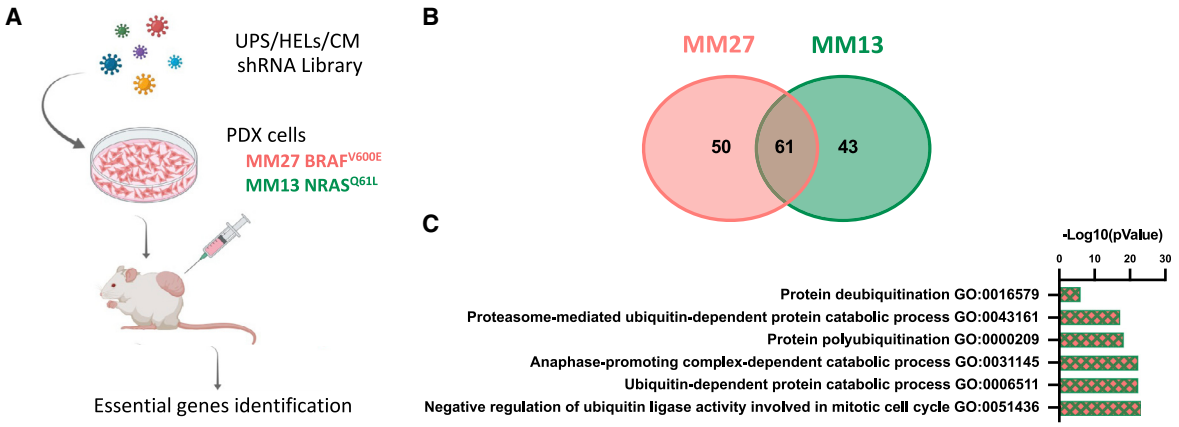

D

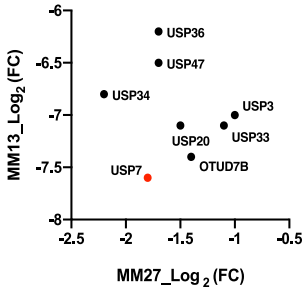

	Log2FC		Ranking	
	MM27	MM13	MM27	MM13
USP7	**-1.8**	**-7.6**	**2**	**1**
USP34	-2.2	-6.8	1	6
USP36	-1.7	-6.2	3	8
USP47	-1.7	-6.5	4	7
USP20	-1.5	-7.1	5	3
OTUD7B	-1.4	-7.4	6	2
USP33	-1.1	-7.1	7	4
USP3	-1.0	-7.0	8	5

E

F

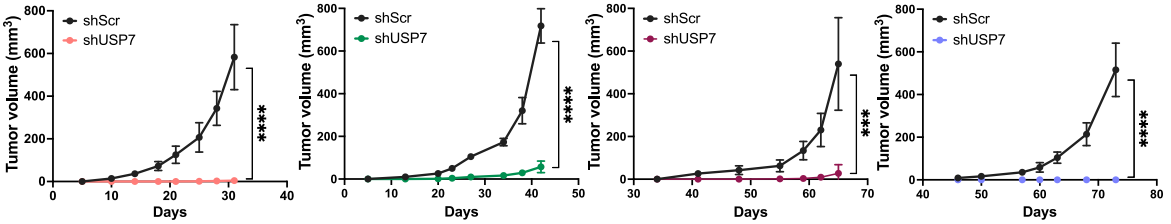

G

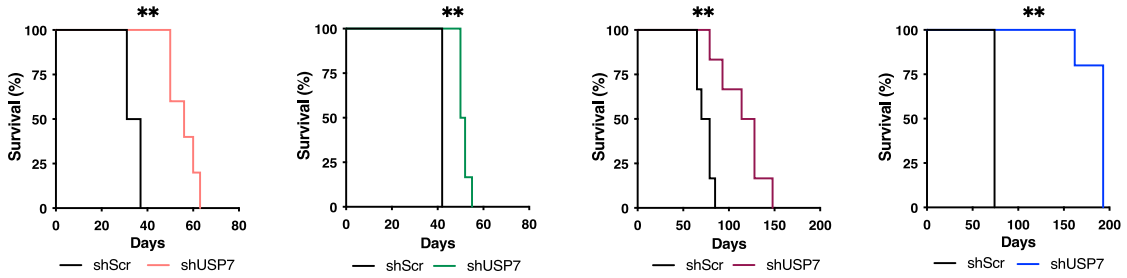

(legend on next page)

2012), but no DUBs regulating RRM2 stability have been described so far. We demonstrate that USP7 knockdown increases RRM2 ubiquitination and decreases RRM2 steady-state levels in S phase, providing another layer of regulation of RRM2. We show that the USP7/RRM2 axis has a pro-tumorigenic role in melanoma.

Cellular senescence can be beneficial or detrimental in tumors (Schosserer et al., 2017). Therapy-induced senescence (TIS) can lead to unfavorable outcomes, promoting drug resistance and disease relapse. Senescent cells remodel their epigenomes (Paluvai et al., 2020); overexpression of histone deacetylase 1 (HDAC1) causes senescence in melanocytes (Bandyopadhyay et al., 2007), and HDAC inhibitors induce apoptosis in melanoma (Yeon et al., 2020). We show that the senescence phenotype depends on HDAC activity. Similarly, LSD1, a member of the lysine-specific histone demethylase family, has been reported to override senescence, and its inhibition suppresses colony formation and melanoma xenograft growth (Lian et al., 2013). Here we report that the pro-senescent effect exhibited by the USP7 inhibitor P5091 can be efficiently targeted by the dual HDAC/LSD1 inhibitor domatinostat, suggesting a new combination therapy for melanoma.

RESULTS

An *in vivo* loss of function screen identifies USP7 as an oncogenic driver in individuals with melanoma

To identify novel targets of melanoma maintenance, we performed *in vivo* loss-of-function shRNA screening in melanoma PDX samples. A shRNA barcoded library targeting 289 ubiquitin proteasome-, helicase-, and metabolism-related genes (see STAR Methods and Table S1 for details) was used to screen two metastatic melanoma PDXs carrying BRAF (MM27) or NRAS (MM13) mutations.

PDX cells were transduced with the shRNA library and then subcutaneously transplanted into immunocompromised non-obese diabetic (NOD).Cg-Prkdc^{scid} Il2rg^{tm1Wjl}/SzJ (NSG) mice, as reported previously (Bossi et al., 2016). Genomic DNA of cells transduced *in vitro* (reference) and tumors grown *in vivo* were sequenced and analyzed for shRNA representation (Figure 1A). The library complexity was fully represented in each tumor, with a high correlation among tumor replicates (Figure S1A). Depleted shRNAs were identified (Figure S1B), and targeted genes were defined as essential during melanoma growth, as described previously (Bossi et al., 2016). We identified 61 hits in common among MM27 and MM13 PDXs (Figure 1B; Table S1) whose Gene Ontology analysis showed robust enrichment of genes of the ubiquitin system; in particular, DUBs involved in cell cycle regulation (Figure 1C; Table S2). We found eight highly depleted ubiquitin-specific proteases (USPs); USP7 was the most depleted in the two PDXs (Figure 1D).

ShUSP7-transduced MM27 and MM13 cells were transplanted into NSG mice (Figure 1E). USP7 knockdown significantly inhibited *in vivo* tumor growth in both PDXs and in two additional samples from affected individuals, MM25 (BRAF mutant) and MM16 (NRAS mutant) (Figure 1F), resulting in significantly increased mouse survival (Figure 1G).

These data demonstrate that USP7 functions as an oncogene in melanoma, independent of the genetic background.

USP7 loss suppresses melanoma proliferation, results in defective G1/S transition, and induces cell senescence *in vitro*

In vitro USP7 depletion induced a profound reduction in cell proliferation in MM27 and MM16 PDX cells (Figure 2A) as well as in MM25 and MM13 PDX cells (Figure S1C). Bromodeoxyuridine (BrDU)-pulsed shUSP7 cells displayed a significant increase in the percentage of G1-blocked cells and a decreased number of cells in S phase (Figures 2B and S1D).

Levels of p21 were significantly increased in shUSP7 PDXs (Figure 2C), whereas cell cycle-regulated cyclins (Figure S1E) and Ki67 expression were markedly decreased (Figure 2C). In tumor cells, USP7 inhibition is known to cause dysregulated cell cycle progression, mainly inducing apoptosis (Peng et al., 2019). In our models, depletion of USP7 instead showed very low levels of cleaved caspase-3/7 (Figure 2D) and PARP-1 (Figure 2E), demonstrating that USP7-depleted cells do not undergo apoptosis.

shUSP7 MM27 and MM16 PDX cells showed a senescent phenotype with large and flattened cell morphology, reduced Lamin B1 levels, and increased SA-β-galactosidase (β-gal) expression (Figure 2F). Senescence-associated secretory phenotype (SASP) proteins were highly produced in shUSP7 cells (Figure 2G). Induction of senescence was confirmed using single USP7 shRNAs (Figures S2A–S2E). The shUSP7-dependent senescent phenotype was also detected in MM25 and MM13 PDXs (Figure S1F).

Functional interrogation of the USP7 depletion phenotype at multiple levels

Because the senescent phenotype induced by USP7 loss has not been described previously in melanoma, we investigated

Figure 1. *In vivo* shRNA screening identifies USP7 as an oncogenic driver in metastatic melanoma

(A) Schematic of the *in vivo* shRNA screening performed in MM27 and MM13 PDX cells transduced with an shRNA library targeting the ubiquitin proteasome system (UPS), helicases (HELs), and cell metabolism (CM)-related genes. Essential genes of melanoma tumor growth were identified.

(B) Venn diagram reporting the number of genes scoring as *in vivo*-depleted genes in MM27, MM13, and in common.

(C) GO functional enrichment analysis of the common depleted genes in MM27 and MM13 PDXs. The representative enriched biological processes are shown in the bar chart with significance of enrichment (–log10 [p value]).

(D) Dot plot showing log_2FC of the 8 DUBs in common between MM27 and MM13. The specific value of log_2FC of each DUB is reported in the table for both PDXs together with the rank order.

(E) Immunoblots of shScramble (shScr), shUSP7 MM27, MM13, MM25, and MM16 PDXs probed for USP7 before cell transplantation.

(F) Effect of USP7 depletion on tumor growth in several PDXs . Tumor volume growth over time is represented as mean ± SD – mm^3 (n = 5 or 6 mice per group). Statistical significance was determined at the last tumor size measurement using an unpaired Student's t test: ***p < 0.001; ****p < 0.001.

(G) Kaplan-Meier curves of shScr and shUSP7 groups (n = 5/6).

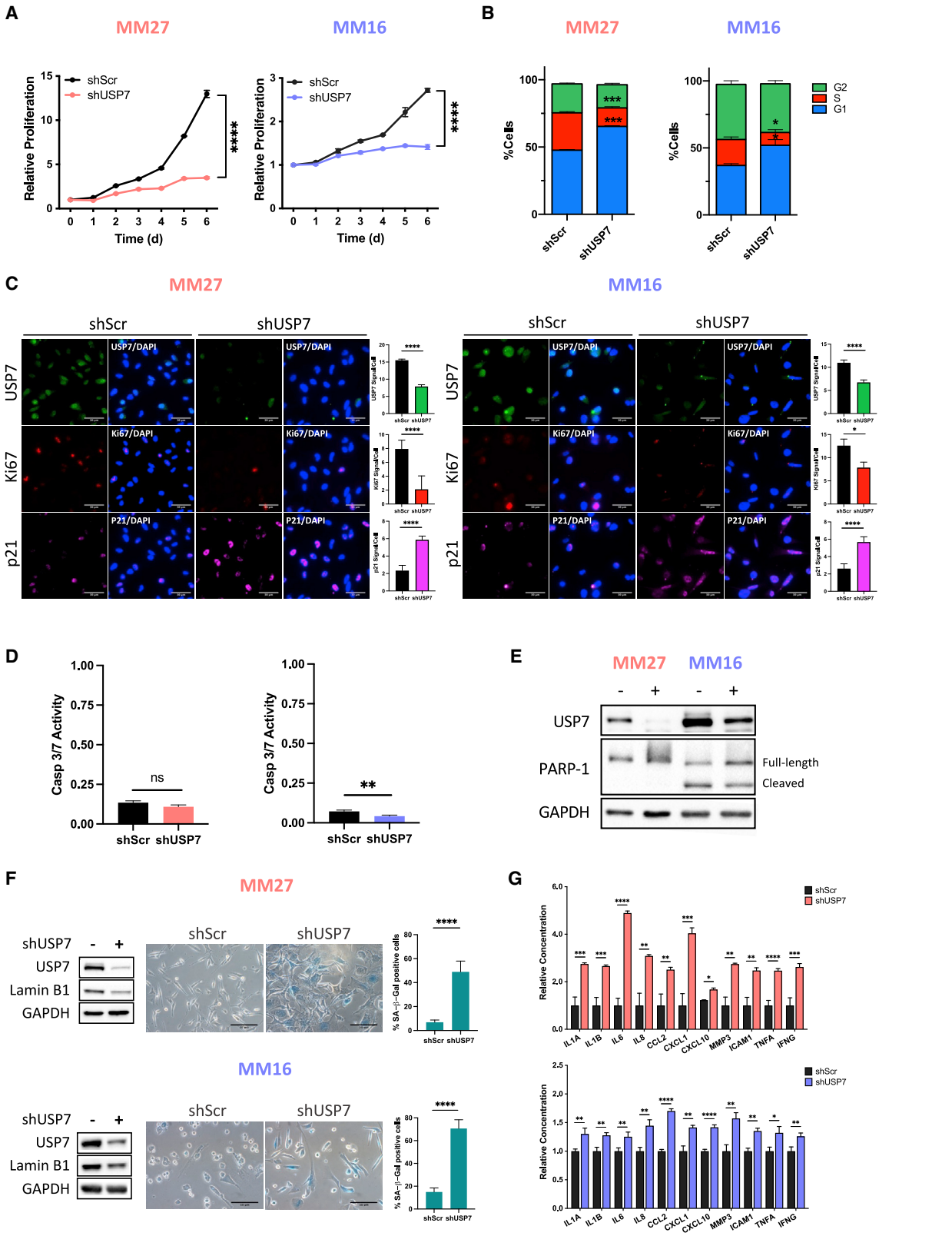

(legend on next page)

the underlying molecular mechanisms by interrogating global transcriptomics and proteomics profiles of shUSP7 MM27 and MM16 samples. We identified many differentially expressed genes (DEGs) (Figure S3A) and differentially expressed proteins (DEPs), either upregulated or downregulated (Figure S3B; Table S3).

In both PDXs, Gene Ontology (GO) functional enrichment analysis of downregulated DEGs showed significant enrichment of categories related to G1/S transition, DNA replication, and replication fork processing. Type I interferon signaling was enriched in upregulated DEGs (Figure 3A). Type I interferon is implicated in induction of cellular senescence in fibroblasts (Tahara et al., 1995). Regulators of cell adhesion and protein polyubiquitination were enriched among upregulated DEPs; factors involved in DNA replication and G1/S transition of the cell cycle were enriched among downregulated DEPs. We found targets significantly regulated at the RNA and protein levels in MM27 and MM16 (Figure S3C). Thus, transcriptomics and proteomics analyses of USP7-depleted cells are consistent with the senescent phenotype observed *in vitro*. Validation of the top commonly regulated genes in the two PDXs is shown in Figure S3D.

To unveil the transcriptional regulators involved in shUSP7-dependent senescence, we analyzed the common upstream regulators in the two PDXs by performing Ingenuity Pathway Analysis (IPA). The most significantly downregulated DEGs were downstream targets of E2F1, CCND1, and CDK4, known to be inhibited in the senescent phenotype, and of p21 (CDKN1A), which is predicted to be activated during senescence (Figure 3C; Degregori et al., 1995).

To validate the identified IPA key regulators, we analyzed Rb and p21 protein levels in our PDXs, showing that p21 was strongly activated in MM27 and MM16 cells upon USP7 silencing (Figure 3D). $p16^{INK4A}$ expression is frequently upregulated in senescent cells, but it could not be detected in our PDXs because loss of $p16^{INK4A}$ expression is a common trait in melanoma (de Sá et al., 2009; Figure S3E). We observed consistent downregulation of hypo-phosphorylated Rb, mechanistically linked to suppression of E2F1-mediated cell cycle regulation (Degregori et al., 1995; Figure 3D). Gene set enrichment analysis (GSEA) revealed significant inhibition of E2F target genes (Figure S3F). Surprisingly, p53 protein levels were not affected by USP7 inhibition, whereas expression of a known USP7 target, MDM2, was downregulated (Figure 3D), suggesting a p53-independent, MDM2-dependent mechanism of p21 activation (Enge et al., 2009). Although, high γH2AX levels are associated with DNA damage-induced senescence (Siddiqui et al., 2015), γH2AX was not upregulated in shUSP7-senescent PDX cells (Figure 3D).

We then investigated the effects of USP7 depletion on the mTOR pathway. We found decreased phosphorylation of mTOR, S6K, and S6 in shUSP7 MM27 and MM16 cells (Figure 3D) and, accordingly, significant inhibition of the mTORC1 pathway (Figure S3G). These findings were also confirmed in MM25 and MM13 PDXs (Figure S3H).

Overall, our results demonstrate that USP7 depletion affects canonical pathways leading to cellular senescence, including the Rb, p21, and melanoma-specific mTOR pathways. Conversely, other signaling routes to senescence, such as p16, p53, or DNA damage, are not involved.

USP7 stabilizes RRM2 by deubiquitination, protecting it from proteasome-mediated degradation

In response to USP7 knockdown, our proteome analysis identified 18 overlapping hits among MM27 and MM16 cells (Figure S4A), 10 of which were the most differentially expressed (log2 fold change [logFC] > −0.3) (Figure 4A). Using the String database, we determined the protein-protein interaction network of the identified proteins, showing enrichment in biological functions such as DNA replication, cell division, and ubiquitin conjugation (Figure S4B). Among the candidates, UBE2S and POLD1 are known USP7-regulated targets (Bremm et al., 2010; Galarreta et al., 2018). RRM2 emerged as the most commonly downregulated protein, suggesting a novel putative role as USP7 target in melanoma (Figure 4A). We validated the decreased protein levels of RRM2 and two more DEPs (KIF11 and ANLN) in shUSP7 MM27 and MM16 cells (Figure S4C).

Our integrative analysis of the transcriptome and proteome of melanoma cells has shown that the 10 candidates were differentially regulated at transcriptional and proteomics level (Figure S4D). To uncover the most downregulated hits at the protein level, we calculated the logFC ratio of RNA and protein of each candidate. In agreement with our previous results, POLD1 and UBE2S were the common top-ranked proteins, and RRM2 was the third-ranking common hit (Figure S4E), supporting its role as a USP7 target.

Figure 2. USP7 loss suppresses melanoma proliferation, resulting in defective G1/S phase transition and induction of cell senescence *in vitro*

(A) Cell viability of shScr and shUSP7 MM27 and MM16 cells was assessed by CellTiter-Glo . The experiment was performed in triplicate and statistical significance of two biological replicates was determined using Student's t test (****$p < 0.0001$).

(B) Cell cycle analysis (BrdU-PI) of shScr and shUSP7 MM27 and MM16 cells. Bars represent the distribution of the cells in the different phases of the cell cycle . Percentages are expressed as a mean ± SD of two biological replicates. p values are based on a two-tailed Student's t test between the shScr vs. shUSP7 cells in G1 and S phase (unpaired Student's t test: ***$p < 0.001$; *$p < 0.05$).

(C) Immunofluorescence analysis of USP7, Ki67, and p21 expression in shScr and shUSP7 MM27 and MM16 cells. Nuclei were counterstained with DAPI (blue). Representative images are shown (scale bars, 30 μm), and bar graphs display the mean of the signal intensity per cell over the total cell number (n = 8).

(D) Caspase-3 and -7 activity of shScr and shUSP7 PDX cells was measured using the Caspase-Glo 3/7 assay . Data are expressed as mean ± SD of triplicate samples. p values are based on Student's t test (ns, not significant; **$p < 0.01$).

(E) Immunoblots of shScr and shUSP7 PDXs probed for USP7 and full-length/cleaved PARP-1.

(F) Senescence assessment phenotype in PDXs. Immunoblots of shScr and shUSP7 PDXs were probed for USP7 and Lamin B1. Representative images (scale bars, 50 μm) and quantification of SA-β-gal staining (SA-β-gal-positive cells/total cell number) are shown. Mean ± SD of 10 images. p values are based on unpaired Student's t test (****$p < 0.0001$).

(G) Relative concentration/cell number of SASPs (senescence-associated secretory phenotypes) in shScr and shUSP7 PDXs. Data are represented as mean ± SD of two independent experiments. p values are based on Student's t test (*$p < 0.05$; **$p < 0.01$, ***$p < 0.001$; ****$p < 0.0001$).

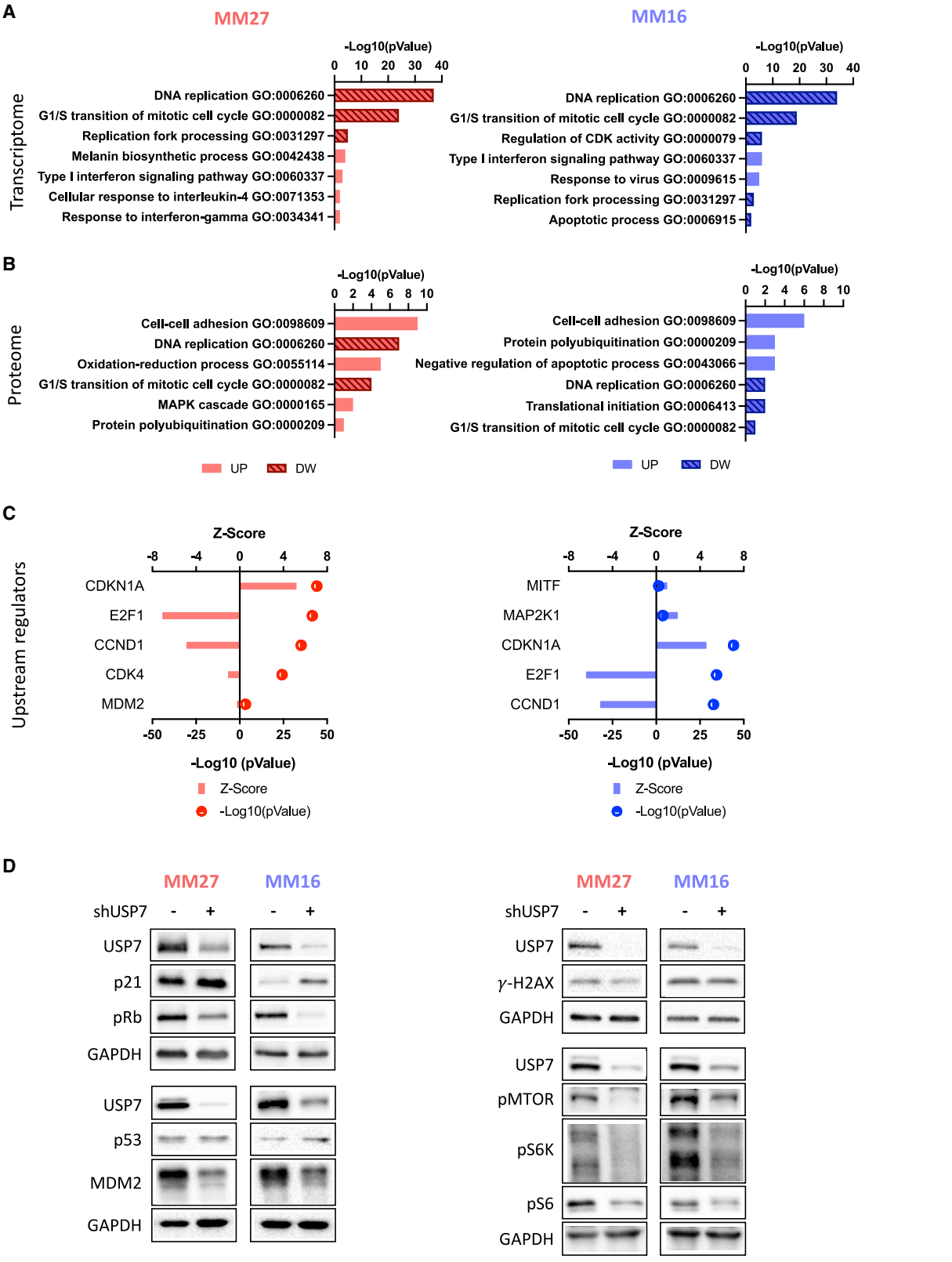

(legend on next page)

To prove whether USP7 regulates RRM2 acting as an inhibitor of its degradation, we treated MM27 cells with the proteasome inhibitor MG132. Strikingly, RRM2 protein downregulation observed in shUSP7 cells was efficiently blocked by MG132 treatment (Figure 4B), suggesting that USP7 affects RRM2 proteasome-mediated degradation, likely by deubiquitinating RRM2. Similar results were obtained with the MM25 and MM16 PDXs (Figure S5A).

We detected polyubiquitination of endogenous RRM2 only after MG132 inhibition, likely because of the fast turnover of the polyubiquitinated protein (Figure 4C). A further increase of RRM2 polyubiquitination in USP7-depleted cells compared with MG132-treated control cells showed that USP7 regulates the RRM2 ubiquitination status through deubiquitination (Figure 4C).

RRM2 expression is cell cycle regulated, peaking in S phase (Chabes et al., 2004), but no such regulation is known for USP7. Therefore, we examined RRM2 and USP7 expression in each phase of the cell cycle by immunofluorescence, synchronizing MM27 cells by double thymidine block and assessing each cell cycle phase by propidium iodide (PI) staining (Figure S5B). RRM2 is temporally regulated, and its expression increased during G1/S phase, peaked in S phase, and drastically decreased in G2 phase, in agreement with its described role in promoting S phase entry (Degregori et al., 1995). In contrast, USP7 levels did not show a strong fluctuation of protein levels during the cell cycle (Figure S5C), as confirmed by western blotting (Figure S5D).

Next we tested whether shUSP7 affects RRM2 ubiquitination in S phase. USP7-depleted, S phase-synchronized cells, treated with MG132 or left untreated, showed an increase in the ubiquitination level of endogenous RRM2 with or without MG132 (Figure 4D). This suggests that high levels of RRM2 during S phase are sustained by the DUB activity of USP7.

Regulation of RRM2 polyubiquitination and degradation by USP7 should lead to significant changes in RRM2 protein half-life. To assess this hypothesis, a cycloheximide (CHX) chase experiment was performed in USP7-depleted and control cells in unsynchronized and S phase-synchronized cells. As shown in Figures 4E and 4A, faster degradation of RRM2 protein was detected upon USP7 depletion only when the cells were S phase synchronized. These results indicate that USP7 regulates RRM2 stability mainly in S phase by preventing proteasomal degradation through deubiquitination.

Then, to investigate USP7 and RRM2 interaction, we performed co-immunoprecipitation assays in unsynchronized and S phase-synchronized RRM2-overexpressing and control MM27 cells (Figure 4F). In unsynchronized cells, USP7 was barely detectable in RRM2-overexpressing cells, whereas in S phase-synchronized cells, increased levels of USP7 co-immunoprecipitated with RRM2 in cells expressing endogenous levels of RRM2. The interaction increased further upon RRM2 overexpression. We then performed a protein ligation assay (PLA) (Alam, 2018) and found a low number of PLA-positive puncta in unsynchronized cells that robustly increased in S phase-synchronized cells (Figure 4G).

These data demonstrate that USP7-RRM2 interaction occurs predominantly in S phase and suggest a new role for USP7 in regulating cell cycle progression by modulating RRM2 protein levels throughout S phase.

ShUSP7-induced senescence is driven by RRM2

Our findings suggest that USP7 modulates melanoma cell proliferation through RRM2 regulation. To better address this, we showed that RRM2-depleted MM27 cells accumulate in G1 phase, reducing the number of S phase cells (Figures 5A and S6A), displaying a similar percentage of SA-β-gal-positive cells as detected in shUSP7 (45.8% and 40.3%, respectively) (Figure 5B). We could not detect increased apoptosis in shRRM2 cells, as shown by unmodified cleaved caspase-3/7 activation (Figure 5C). The shRRM2 senescent phenotype was also confirmed by SA-β-gal staining in all PDXs (Figure S6B). We then investigated the senescence-associated pathways in shUSP7 and shRRM2 cells. As expected, p21 was upregulated and pRb downregulated (Figure 5D; quantification illustrated in Figure S6C), strengthening the hypothesis that the functional crosstalk between USP7 and RRM2 regulates the same pathways.

We investigated whether a shUSP7-mediated cell cycle block could be rescued by ectopic expression of RRM2. As shown in Figures 5E and S6D, USP7 knockdown suppressed cell cycle progression, reducing the percentage of S phase cells (from 32.9% to 13.6%), whereas RRM2 restoration significantly reversed the effect of USP7 depletion, increasing S phase cells up to 26.3%. RRM2 overexpression in USP7-depleted cells reversed the downregulation of pRb and activation of p21 Figure 5F) and reduced the SA-β-gal positivity caused by USP7 knockdown from ∼30% to 10% (Figure 5G).

p21 knockdown partially rescued the shUSP7-mediated, SA-β-gal-positive phenotype (Figure S6E) through restoration of pRb and RRM2 levels (Figure S6F), suggesting a pivotal role of p21 in mediating shUSP7-induced senescence.

These findings demonstrate that USP7 regulates G1/S phase transition via RRM2 stabilization, proposing USP7 as a promising therapeutic target in melanoma.

USP7 expression correlates with a dismal prognosis in individuals with melanoma

We analyzed the expression of USP7 in a large cohort of individuals with primary melanoma by tissue microarray analysis (TMA). A total of 143 archival paraffin-embedded melanoma samples were considered in the study, including all melanoma stages (Table S4). We found that USP7 expression correlated with progression (Figure 6A), and, more importantly, high expression of

Figure 3. Transcriptomics and proteomics analyses of USP7-depleted MM27 and MM16 cells reveal multiple deregulated pathways

(A and B) RNA sequencing (RNA-seq; A) and mass spectrometry (B) analyses were performed on shScr and shUSP7 MM27 and MM16 cells. The bar chart shows representative Gene Ontology (GO) enriched biological process terms associated with upregulated (UP) and downregulated (DW) DEGs.

(C) Ingenuity Pathway Analysis (IPA) identifies significant upstream regulators (UR) of DEGs. URs are analyzed by *Z* score (activated, greater than 2, inhibited, less than −2) in bars and significance of enrichment (–log10 p value) in dots.

(D) Investigation of downstream pathways affected by shUSP7 in MM27 and MM16 cells. Cell lysates were immunoblotted with the indicated antibodies.

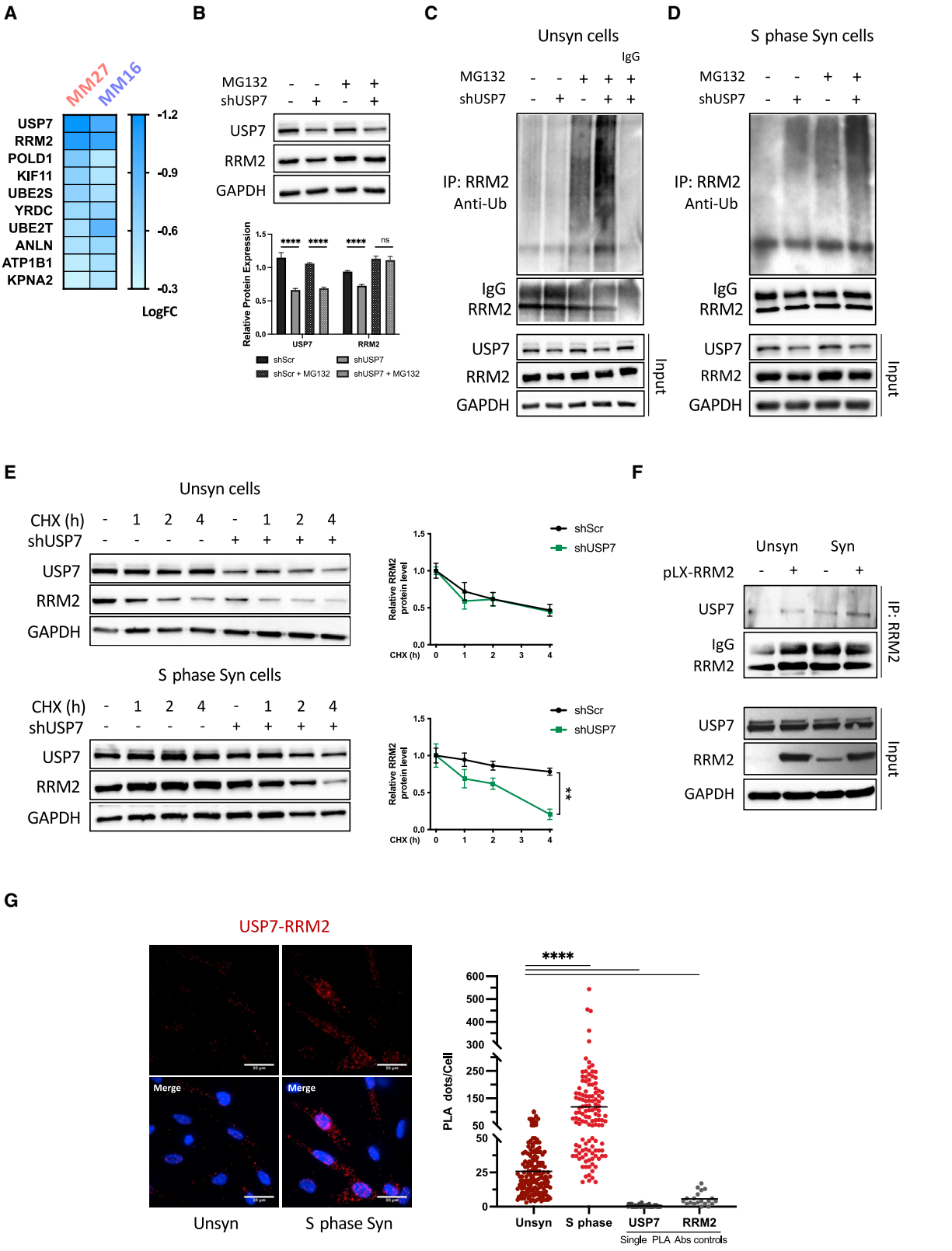

(legend on next page)

USP7 was significantly associated with all main prognostic factors (immunohistochemistry [IHC] score 3; STAR Methods; Figure 6B). Melanomas highly expressing USP7 were significantly thicker (68.42% of affected individuals showed a Breslow's thickness greater than 4mm versus 31.58% among the USP7-low melanomas, $p = 0.008$), with a greater number of mitotic events (66.07% among USP7-high versus 33.93% among USP7-low, $p < 0.0001$) and more invasive (Clark's level V was 75% among USP7-high versus 25% among USP7-low, $p < 0.0001$) (Figure 6B). USP7 expression was also associated with tumor stage; the majority of advanced-stage individuals were high USP7 expressors ($p = 0.024$). These findings strengthen the association of USP7 expression with a more aggressive melanoma phenotype.

Within our cohort of primary melanomas, 35% of the individuals died with a median follow-up of 100 months (Table S4), and we found significant worse overall survival (log rank $p = 0.0139$) among the individuals displaying high levels of USP7 (Figure 6C). Disease-free survival (log rank $p = 0.0010$) was also significantly worse in high USP7-expressing tumors compared with low USP7-expressing melanomas (Figure 6D).

These data suggest that USP7 is a novel prognostic factor in melanoma, conferring an unfavorable outcome for individuals with melanoma.

Combination treatment with a USP7 inhibitor and HDAC/LSD1 inhibitor induces additive anti-melanoma activity

Because USP7 is a druggable therapeutic target (Zhou et al., 2018), we first tested the efficacy of the USP7 inhibitor P5091 on MM27 PDX cell proliferation, showing that it was significantly suppressed in a dose-dependent manner (Figure S7A) and maintained over time (Figure S7B). Cell viability was strongly reduced in P5091-treated MM27 PDX cells after 48 h (Figure 7A). Treated cells exhibited G1 phase accumulation (Figures 7B and 7S7C) and SA-β-gal positivity (Figure 7C) associated with a p21 level increase and Rb hypo-phosphorylation (Figure 7D), phenocopying the shUSP7-induced phenotype. As expected, treatment with P5091 did not induce an increased apoptosis rate in MM27 cells, as shown by measurement of PARP-1 cleavage Figure 7E).

To test P5091 efficacy *in vivo*, MM27 PDX cells were subcutaneously transplanted, and mice were treated with P5091 or vehicle. P5091 treatment inhibited melanoma tumor growth Figure 7F). We characterized tumor samples by IHC analysis, and, in agreement with our *in vitro* findings, we observed downregulation of pRb, Lamin B1. and RRM2 as well as p21 upregulation (Figure 7G). SA-β-gal staining showed that P5091-treated tumors were β-gal positive (Figure 7H). These data corroborate the pro-senescence effect of USP7 inhibition.

H3 global acetylation analysis in P5091-treated cells displayed overall H3 hypo-acetylation, indicative of strong deacetylase activity of HDAC proteins (Figure S7D). To clear senescent cells, MM27 was treated with P5091, followed by administration of the HDAC/LSD1 dual inhibitor domatinostat. Each single treatment significantly reduced cell viability (~40%), which was further reduced with the combination treatment (~75%) (Figure 7I).

Although P5091 did not cause cell death, domatinostat was able to induce a 5-fold increase in cell toxicity, which increased to 10-fold with the combination treatment (Figure 7J), suggesting activation of specific apoptosis signals, as detected by the highest ratio of PARP-1 cleavage (Figure 7K). P5091 and domatinostat combination induced p53 activation and increased γH2AX expression, suggesting DNA damage as a putative trigger of apoptosis (Figure 7L). Cells treated with the drug combination also showed increased H3 acetylation (Figure S7E), supporting a critical role of HDAC activity in clearing senescent cells. A similar additive effect was assessed, combining P5091 with other HDAC inhibitors, vorinostat and belinostat (Figure S7F). The efficacy of P5091 combined with all three epigenetic inhibitors was also confirmed in MM16 PDX cells (Figure S7G). We confirmed the potency of this drug combination by using more recent USP7 inhibitors, FT671 (Turnbull et al., 2017) and GNE6640 (Kategaya et al., 2017), in MM27 and MM16 cells (Figure S7H).

To explore the therapeutic efficacy of the P5091 and domatinostat combination, MM27 PDX cells were subcutaneously injected into NSG mice. When tumors reached a size of about 80 mm^3, animals were treated with vehicle, P5091, domatinostat, or the combination of the two drugs. The combination elicited strong growth inhibition, whereas single drug treatment showed modest anti-tumor effects (Figures 7M and 7N). No body weight reduction was observed in any treatment group (Figure 7O), indicating good tolerability of this novel drug combination.

Figure 4. USP7 depletion regulates RRM2 stability by increasing RRM2 ubiquitination

(A) Heatmap of the top downregulated proteins in USP7-depleted MM27 and MM16 cells. Top-ranking genes from the proteome profile are indicated ($log_2FC > -0.3$, $p < 0.05$).

(B) RRM2 protein stability was assessed by western blot in the presence or absence of the proteasome inhibitor MG132 in shScr and shUSP7 MM27 cells. Bar graphs show quantification of protein levels normalized against GAPDH . Protein levels are expressed as a mean ± SD of three independent experiments. p values are based on Student's t test (****$p < 0.0001$; ns, not significant).

(C and D) Western blots of the total lysates (input) and immunoprecipitates (IP) of RRM2 from shScr and shUSP7 unsynchronized (Unsyn, C) and S phase-synchronized (Syn, D) MM27 cells, untreated/MG132 treated. Blots were probed with an anti-Ub and RRM2 antibody. An immunoglobulin G (IgG) antibody was used as an IP control.

(E) ShScr and shUSP7 Unsyn (top panel) and S phase Syn (bottom panel) MM27 cells were treated with cycloheximide (CHX). Cells were harvested and immunoblotted with USP7 and RRM2 antibodies at the indicated time points. Line charts show quantification of RRM2 levels normalized to GAPDH and to an untreated control of each group . Mean ± SD of three independent experiments. Unpaired Student's t test: **$p < 0.01$.

(F) Western blots of the total lysates (input) and IP of overexpressing RRM2 or control from Unsyn and S-phase Syn MM27 cells. Blots were probed with USP7 and RRM2 antibodies.

(G) RRM2/USP7 *in situ* protein interactions. Shown is a proximity ligation assay of RRM2 and USP7 in Unsyn and S phase Syn MM27 cells. Nuclei were counterstained with DAPI (blue). Representative images (scale bars, 30 μm) are shown, and quantification (n = 5) of PLA is expressed as number of fluorescent/dot. Control conditions are reported with each primary antibody. Data are mean ± SD. p values are based on unpaired Student's t test (****$p < 0.0001$).

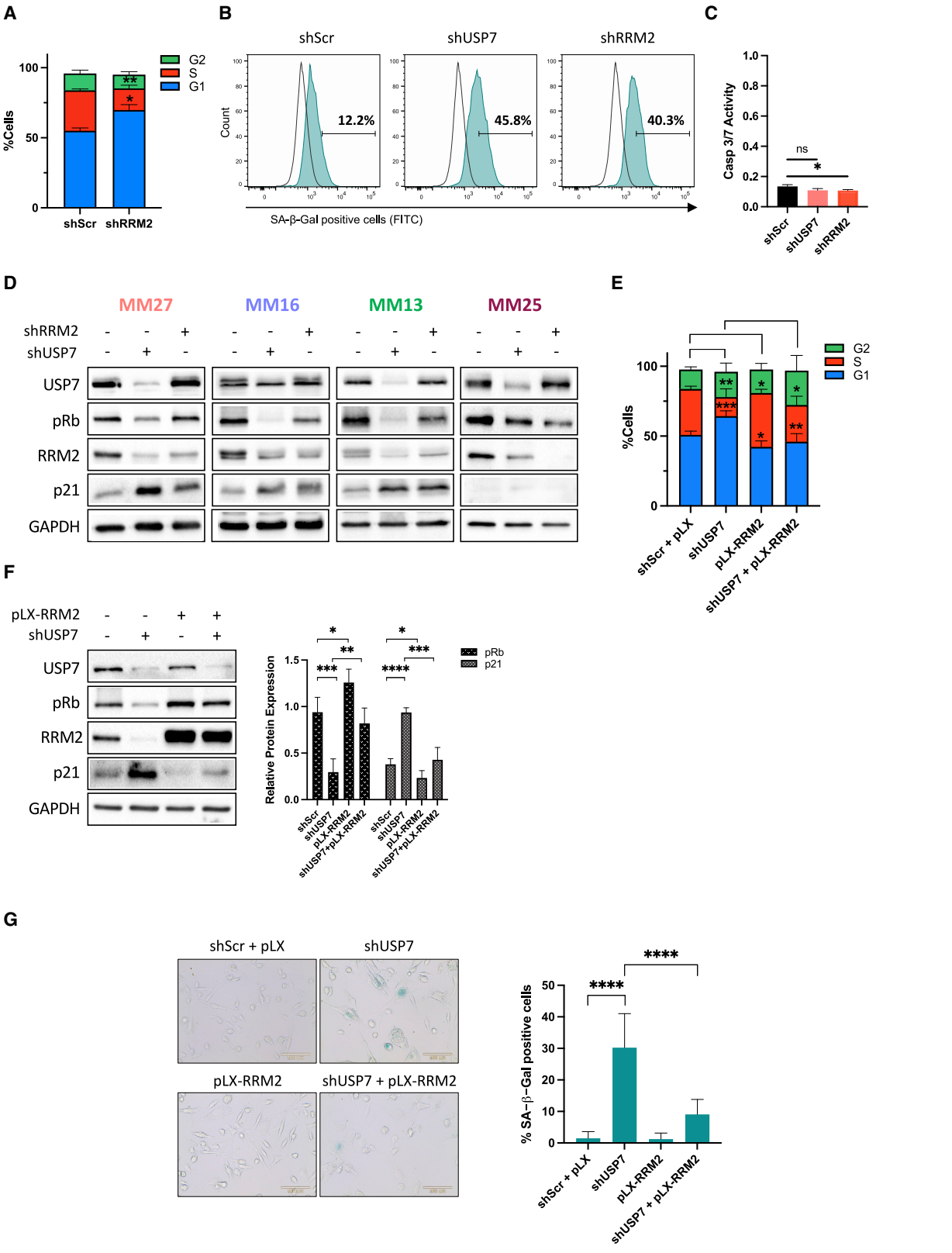

(legend on next page)

We observed a robust reduction of SA-β-gal-positive cells in tumors treated with the drug combination, proving the senolytic activity of domatinostat (Figure 7P). In these tumors, we also detected activation of γH2AX and increased cleaved caspase-3 levels (Figure 7Q), which suggests that the treatment induces DNA damage and, consequently, apoptosis, consistent with our *in vitro* findings.

Our combination treatment provides a rationale for development of USP7-based therapies to improve melanoma outcomes. We show that combination treatment with domatinostat can efficiently remove senescent cells, inducing cytotoxicity via DNA damage activation, suggesting its use in TIS in melanoma.

DISCUSSION

Because targeting key vulnerabilities is an attractive approach to developing cancer-selective therapeutic agent, we conducted an *in vivo* dropout screen in BRAF- and NRAS-mutant melanoma PDXs using a pooled shRNA library targeting UPS-, helicase- and cell metabolism-related genes. The rationale for using shRNA-based libraries stemmed from the necessity of suppressing gene function without abolishing it completely to better mimic the action of therapeutic drugs in affected individuals (Bossi et al., 2016).

Most tumors, including melanomas, show alterations in cell cycle progression and, thus, uncontrolled proliferation (Hanahan and Weinberg, 2000). In this study, we focused our attention on DUBs, which play key roles in cell cycle regulation (Park et al., 2019) and whose oncogenic and tumor-suppressive functions have been deeply investigated in the last decade, raising interest in their targeting (D'arcy et al., 2015; Li and Reverter, 2021). We identified a set of DUBs critical for development of BRAF- and NRAS-mutant melanomas, which are known to predict clinical outcome in others malignancies (Nijman et al., 2005; Huang and Dixit, 2016). Here we studied the top-ranked inhibited gene, USP7, which plays a crucial role in tumorigenesis in several cancers: high USP7 levels have been documented in many cancers and recently also in melanoma (Xiang et al., 2021; Vishnoi et al., 2018; Gao et al., 2021). However, its mechanism of action has not yet been uncovered yet.

By performing USP7 loss-of-function studies, we proved that USP7 inhibition halts melanoma growth *in vivo* and arrests cell proliferation *in vitro*. USP7 inhibition triggers p53-dependent apoptosis in cancer cells (Mungamuri et al., 2016; Zhou et al., 2018; Gao et al., 2021) as well as in senescent fibroblasts (He et al., 2020), mainly in response to DNA damage (Zhu et al., 2015; Minmin et al., 2021; Xiang et al., 2021). Conversely, neither apoptosis nor DNA damage could be detected in our cells upon shUSP7 or P5091 treatment. In our PDXs, known to better recapitulate the genetic and functional heterogeneity melanoma tissues than cell lines (Bossi et al., 2016), USP7 loss drives senescence.

It has been shown previously that activation of the mTOR pathway is required to bypass BRAF-dependent oncogene-induced senescence in melanoma (Damsky et al., 2015) and that mTOR inhibition is critical for TIS (Yoshida et al., 2016). Here we show that downregulation of the mTOR pathway is one of the features of shUSP7-induced senescence, suggesting that activation of this pathway could be a putative way out to reactivate proliferation.

To uncover the mechanism underlying induction of senescence in our melanoma PDXs, we investigated the early cascade of proteomic and transcriptomic changes induced by USP7 depletion. Functional analysis identified DNA replication and cell cycle regulation as top-ranked biological processes. We can propose a scenario shared by melanomas with different genetic backgrounds and phenotypic features, where loss of USP7 induces p53- and p16-independent senescence through p21 upregulation and Cyclin D-CDK4/6 inhibition, which prevents Rb phosphorylation, suppressing genes essential for G1/S phase transition and DNA replication, mainly driven by E2F1.

Replication fork processing and DNA replication were over-represented biological functions in our GO analysis. USP7 regulates fork progression and origin firing in a p53-independent way during DNA replication (Lecona et al., 2016) and specifically modulates the stability of known components of the replisome, such as members of the MCM complex (UHRF1, DNMT1, and POLD1; Qin et al., 2011; Sowa et al., 2009), one of the main downregulated proteins in our proteome analysis. Based on these observations, we can speculate that depletion of USP7 could lead to a cell cycle block by inducing a stalled replication fork in our PDXs. Replicative stress can be accompanied by DNA damage, but senescence can also occur in the absence of it (Bielak-Zmijewska et al., 2018). We did not detect

Figure 5. Cellular senescence induced by USP7 depletion is driven by RRM2

(A) Cell cycle analysis (BrdU-PI) of shScr and shRRM2 MM27 cells. Bars represent the distribution of the cells in the different phases of the cell cycle . Mean ± SD of two biological replicates. p values are based on unpaired Student's t test of shScr vs. shRRM2 cells in G1 and S phase (**p < 0.01; *p < 0.05).

(B) SA-β-gal activity was quantified by flow cytometry in shScr, shUSP7, and shRRM2 MM27 cells. Histograms of each condition compared with an unstained control are shown, and SA-β-gal positivity is expressed as a percentage (n = 2).

(C) Activation of caspase-3 and -7 in shScr, shUSP7, and shRRM2 MM27 cells was measured using the Caspase-Glo 3/7 assay . Data are expressed as mean ± SD of triplicate samples. ns, not significant; *p < 0.05.

(D) Immunoblots of shScr, shUSP7, and shRRM2 in four PDXs were probed for the indicated proteins.

(E) Cell cycle analysis (BrdU-PI) of USP7-depleted and/or RRM2 overexpressing (pLX-RRM2) MM27 cells. Bars represent the distribution of the cells in the different phases of the cell cycle . Percentages are expressed as a mean ± SD of three biological replicates. p values are based on unpaired Student's t test between all samples vs. control in G1 and S phase (***p < 0.001; **p < 0.01; *p < 0.05).

(F) Western blot of USP7-depleted and/or RRM2-overexpressing (pLX-RRM2) MM27 cells were probed for the indicated proteins. Bar graphs show quantification of protein levels normalized against GAPDH . Protein levels are expressed as a mean ± SD of three independent experiments. Unpaired Student's t test: ***p < 0.001; **p < 0.01; *p < 0.05.

(G) SA-β-gal staining of USP7-depleted and/or RRM2 overexpressing MM27 cells. Representative images (scale bars, 100 μm) are shown. Bar graph shows quantification of SA-b-Gal-positive cells (10 images, mean ± SD). p values are based on Student's t test (****p < 0.0001).

A

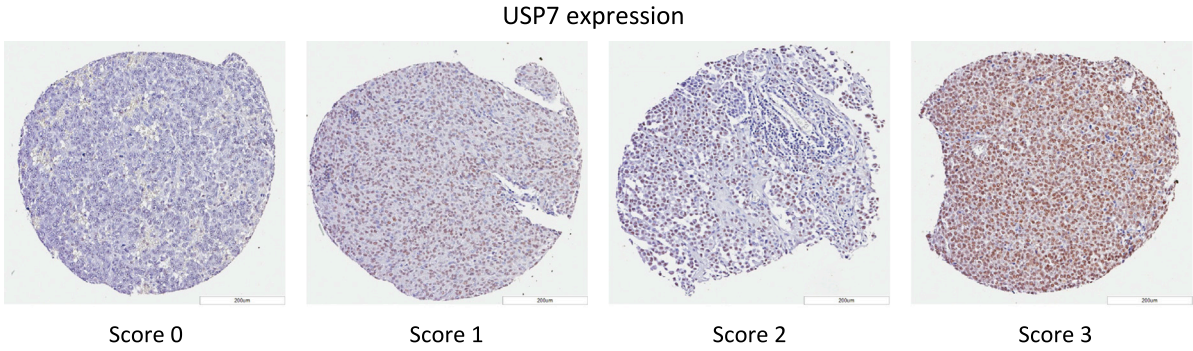

B

		USP7 LOW (N and %)	USP7 HIGH (N and %)	Pearson χ2
Stage	I	33 (64.71%)	18 (35.29%)	
	II	4 (33.33%)	8 (66.67%)	**P=0.024**
	III	8 (40%)	12 (60%)	
	IV	0	3 (100%)	
Breslow	T1	34 (68%)	16 (32%)	
	T2	3 (25%)	9 (75%)	
	T3	6 (50%)	6 (50%)	**P=0.008**
	T4	6 (31.58%)	13 (68.42%)	
Clark	II	32 (80%)	8 (20%)	
	III	6 (37.5%)	10 (62.5%)	
	IV	8 (28.57%)	20 (71.43%)	**P<0.0001**
	V	2 (25%)	6 (75%)	
Tumor Mitotic rate	<1	27 (81.82%)	6 (18.18%)	
	≥1	19 (33.93%)	37 (66.07%)	**P<0.0001**
Ulceration	ABS	34 (53.97%)	29 (46.03%)	
	PRES	11 (42.31%)	15 (57.69%)	P=0.3170
Vascular Invasion	ABS	40 (54.05%)	34 (45.95%)	
	PRES	3 (42.86%)	4 (57.14%)	P=0.5705
Histotipe	SSM	35 (58.33%)	25 (41.67%)	
	NM	13 (39.39%)	20 (60.61%)	P=0.0803
Lymph node Metastases	NO	39 (60%)	26(40%)	
	YES	8 (38.1%)	13 (61.9%)	P=0.0796
Distant Metastases	NO	47 (59.49%)	32 (40.51%)	
	YES	2 (13.33%)	13 (86.67%)	**P=0.0010**
Status	ALIVE	36 (63.16%)	21 (36.84%)	
	DEAD	13 (35.14%)	24 (64.86%)	**P=0.0079**

C

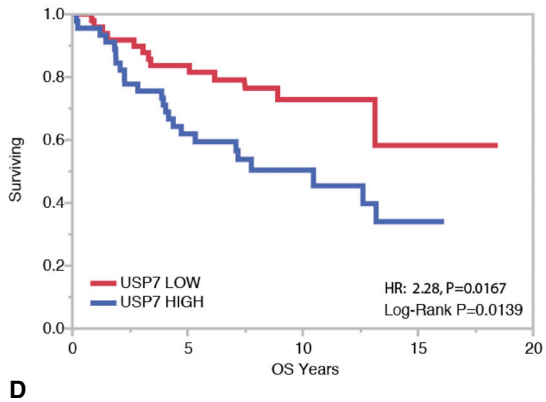

D

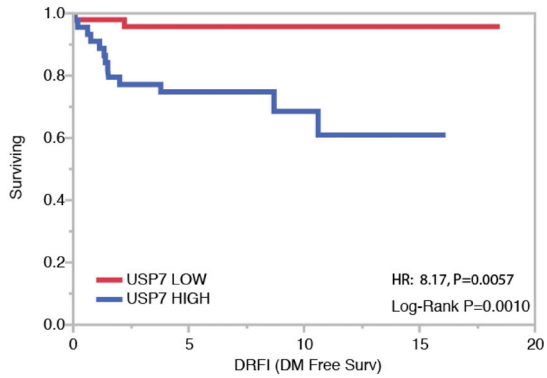

Figure 6. USP7 expression correlates with melanoma progression and poor prognosis in individuals with melanoma

(A) Analysis of USP7 expression by TMA. Images are representative of USP7 expression scoring according to TMA intensity staining. Scale bars, 200 μm.

(B) Correlation of USP7 expression with clinicopathological characteristics of individuals with melanoma.

(C and D) Overall survival (C) and disease-free survival (D) curves of 94 individuals with melanoma with low (red curve) or high (blue curve) USP7 expression.

increased γH2AX level in shUSP7-depleted or P5091-treated cells.

In this work, we demonstrate that USP7 mediates cell cycle progression regulating RRM2 protein expression. Because cancer cells require elevated dNTP levels to sustain the high proliferation rate, RRM2 is frequently deregulated in cancer. Overexpression of RRM2 has been shown in various tumor types (Fatkhutdinov et al., 2016; Rahman et al., 2013; Wang et al., 2014; Mazzu et al., 2019; Zou et al., 2019), suggesting that it may be a downstream effector of multiple cancer-related processes. We identified RRM2 as the most commonly downregulated protein in our USP7-depleted PDXs. Beyond the reported cell cycle regulation of RRM2 by E2F signaling, which was the top upstream regulator in shUSP7 cells, our study demonstrates that RRM2 levels are also regulated by USP7. Using an *in vivo* deubiquitination assay, we demonstrated that RRM2 polyubiquitination was significantly increased upon USP7 knockdown, suggesting that RRM2 is a *bona fide* USP7 substrate.

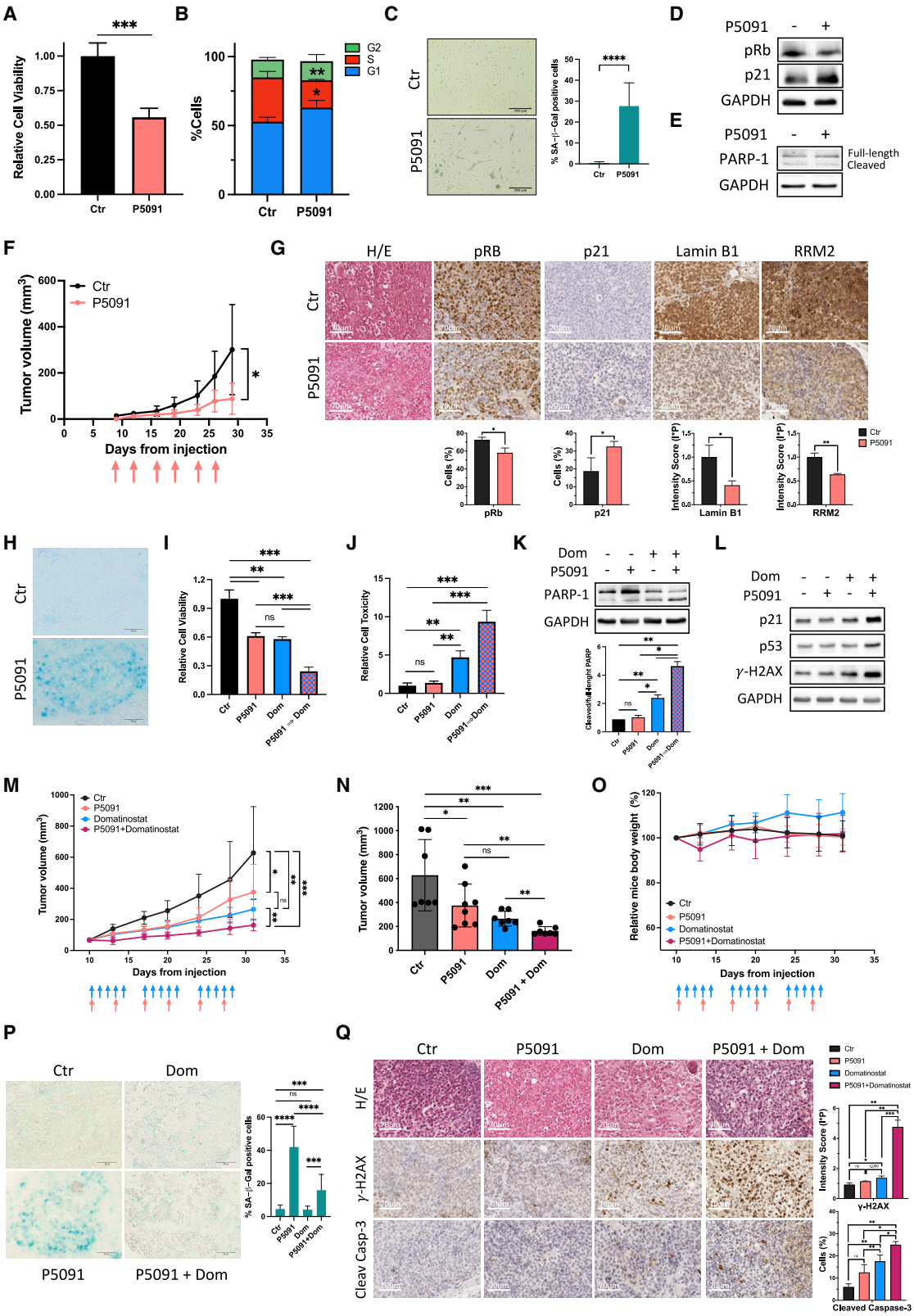

(legend on next page)

This finding was further supported by a recently published USP7 ubiquitinome analysis (data-independent acquisition mass spectrometry; Steger et al., 2021). This study identified increased polyubiquitination of RRM2 at R120 and R180 lysine residues in colon carcinoma HCT116 cells treated with the selective USP7 inhibitor FT671.

We also showed that USP7 directly regulates RRM2 stability mainly in S phase by preventing proteasomal degradation through deubiquitination. In S phase-synchronized shUSP7 cells, where RRM2 levels are more stable or protein turnover is slowed down, we found a pronounced accumulation of RRM2 polyubiquitination regardless of MG132 treatment and a consequent significant instability of the RRM2 steady state in S phase. We demonstrated that USP7 and RRM2 co-immunoprecipitate, displaying the highest interaction during S phase. This is the first report showing USP7/RRM2 interaction, suggesting that USP7 directly regulates RRM2 stability mainly in S phase by preventing proteasomal degradation through deubiquitination.

RRM2 inhibition induces senescence in melanoma (Fatkhutdinov et al., 2016). Specifically, cells that undergo stable oncogene-induced, p16-and p53-independent senescence show decreased RRM2 expression and dNTP levels (Aird et al., 2013; Mannava et al., 2013). We demonstrated that RRM2-depleted PDX cells were G1 blocked and underwent senescence through deregulation of Rb and activation of p21, suggesting that RRM2 affects the same pathways regulated by USP7. RRM2 overexpression was able to rescue the shUSP7-induced senescent phenotype, which can likely be explained by retrieval of replication efficiency, as reported previously (Garzon et al., 2017). Our findings suggest that USP7 controls the proliferation properties of melanoma cells by regulating RRM2 expression.

We can propose a functional dynamic model where USP7 binds RRM2 and regulates its stabilization to guarantee proper DNA replication with regular fork progression, leading to cell proliferation. These results are also consistent with the idea that increased levels of USP7 and RRM2 contribute to melanoma growth. Poor overall survival has been shown in individuals with melanoma overexpressing USP7 or RRM2 (Vishnoi et al., 2018; Gao et al., 2021; Aird et al., 2013). We also showed that low USP7 expression correlates with prolonged disease-free survival.

In the present study, we also evaluated pharmacological inhibition of USP7 with P5091 and demonstrated its efficacy *in vitro* and *in vivo* by inducing senescence. TIS is triggered through extensive DNA damage induced by drug treatment but also independent of it (Saleh et al., 2020). TIS is a therapeutic opportunity to arrest tumor proliferation using low doses of drugs, therefore minimizing side effects in the affected individual. However, TIS exploitation is still highly debated because it can favor accumulation of arrested and therapy-resistant cells promoting tumor recurrence (Demaria et al., 2017).

Hence, it is not surprising that targeted elimination of senescent cells has become a promising new avenue for therapeutic intervention, mainly activating cell death (Von Kobbe, 2019). Senescent cells are characterized by epigenetic alterations that sustain permanent cell-cycle arrest (Paluvai et al., 2020).

Figure 7. Combination treatment of the USP7 inhibitor, P5091, and HDAC/LSD1 inhibitor domatinostat, shows additive anti-melanoma activity *in vitro* and *in vivo*

(A–E) *In vitro* P5091 (5 μM) treatment (48 h) of MM27 cells. (A) Cell viability was assessed by CyQuant and is indicated over control (n = 3). Mean ± SD. p values are based on unpaired Student's t test (***p < 0.0001).

(B) Cell cycle analysis of BrdU-labeled MM27 cells. Bars represent the distribution of the cells in the different phases of the cell cycle. Percentages are expressed as a mean ± SD of three biological replicates. p values are based on unpaired Student's t test between all the samples vs. control in G1 and S phase (**p < 0.01; *p < 0.05).

(C) Representative images of SA-β-gal staining (scale bars, 200 μm) are shown. The bar graph shows quantification of SA-β-gal-positive cells (n = 10). p values are based on unpaired Student's t test (****p < 0.0001).

(D and E) Immunoblots probed for pRb and p21 antibodies (D) and with PARP-1 (E).

(F–H) *In vivo* effect of P5091 treatment (15 mg/kg, intravenously [i.v.]) in an MM27 PDX.

(F) Tumor growth over time is shown (7 mice/group). Mean ± SD. Unpaired Student's t test: *p < 0.05. Arrows indicate treatment administration.

(G) Treated tumors were stained with H&E, pRb, p21, Lamin B1, and RRM2. Representative histopathological images are presented (scale bars, 70 μm). Bar graphs show quantification of stained positive cells (n = 4). For pRb and p21, the stained cells were calculated as percentage over the total tumor cells, and the intensity score (I*P) was calculated for Lamin B1 and RRM2. Mean ± SD of two mice per each group. Unpaired Student's t test: *p < 0.05; **p < 0.01).

(H) Treated tumors were stained with SA-β-gal. Shown are representative images (n = 6) of SA-β-gal staining of tumor sections (scale bars, 50 μm).

(I–L) Effect of P5091 (5 μM) and domatinostat (Dom; 0.35 μM) sequential combination treatment *in vitro*.

(I and J) Cell viability by CyQuant (I) and cell toxicity by CellTox Green cytotoxicity (J) were evaluated (n = 3). Mean ± SD. Student's t test was used to assess significance between each condition (ns, not significant; **p < 0.01; ***p < 0.001).

(K) Western blot analysis showing full-length and cleaved PARP-1 protein. The ratio of cleaved and full-length PARP is plotted as bar graphs (n = 3). Mean ± SD. Student's t test was used to assess significance between each condition (ns, not significant; *p < 0.05; **p < 0.01).

(L) Immunoblot analysis of p21, p53, and γH2AX expression.

(M–Q) Effect of P5091 (15 mg/kg, i.v.) and Dom (60 mg/kg, og) combination therapy *in vivo*.

(M) Tumor growth curves (7–8 mice/group) are reported (mean ± SD). Unpaired Student's t test: ns, not significant; *p < 0.05; **p < 0.01; ***p < 0.001. The arrows indicate treatment administration.

(N) Tumor volumes (3 days after the last treatment). Mean ± SD. Unpaired Student's t test: ns, not significant; *p < 0.05; **p < 0.01; ***p < 0.001.

(O) Body weight was measured upon treatment administration. Mean ± SD.

(P) Treated tumors were stained with SA-β-gal. Shown are representative images (n = 6) of SA-β-gal staining of tumor sections (scale bars, 50 μm). Student's t test: ns, not significant; ***p < 0.001; ****p < 0.0001.

(Q) Treated tumors were stained with H&E, pRb, p21, Lamin B1, and RRM2. Representative histopathological images are presented (scale bar, 70 μm). Bar graphs show quantification of stained positive cells . For γH2AX, the stained cells were calculated as percentage over total tumor cells, and I*P was calculated for cleaved casapse-3. Statistical analyses include 3 mice per group (Student's t test: ns, not significant; *p < 0.05; **p < 0.01; ***p < 0.001).

Overexpression of HDAC1 in melanocytes has been reported to drive activation of a network of chromatin modifiers, ultimately leading to senescence (Bandyopadhyay et al., 2007). In our PDX models, we observed hypo-acetylation of histone H3, reflecting sustained activity of HDAC in senescent cells.

In line with our data, we used domatinostat to target senescent cells, one of the most recent dual inhibitors selectively targeting class I HDACs (HDAC1, HDAC2, and HDAC3) and the lysine-specific histone demethylase 1 (LSD1) (Inui et al., 2017), shown previously to be essential for melanoma progression *in vivo* in our models (Bossi et al., 2016). LSD1 has been shown to override senescence in melanoma (Lian et al., 2013). Domatinostat efficacy in a combination regimen is investigated in recent clinical trials of advanced-stage melanomas (NCT03278665). In our work, we show that the P5091 and domatinostat combination resulted in an additive inhibitory effect on cell viability and, more importantly, on cell death, probably through increased cytotoxicity via DNA damage, promoting senescent cell clearing, in *in vitro* and *in vivo* studies.

Our research highlights the oncogenic role of USP7 in melanoma, providing a mechanistic landscape illustrating the shUSP7-related senescent phenotype. Our findings also establish a central role of the USP7/RRM2 axis in melanoma maintenance. The high levels of USP7 and RRM2 in melanoma confirm the key role of USP7 as a tumor-promoting factor and, therefore, a promising therapeutic target.

This study provides evidence supporting the potential clinical application of combining senescence induction therapies with senolytic therapies in cancer. Our work specifically sheds light on alternative therapeutic options for patients with melanoma, increasing the efficacy of P5091 by targeting the residual senescent cells with domatinostat.

Limitations of the study

Because we provide a new therapeutic strategy for individuals with melanoma, the limitation of our combination is that USP7 inhibitors have not yet been explored in clinical trials, to the best of our knowledge. Therefore, it is highly desirable that the potency as well as the pharmacokinetics and pharmacodynamics properties of USP7 inhibitors are studied and improved for clinical translation.

Even with many intracellular processes ascribed to the deubiquitinating activity of USP7, the mechanism of action of USP7 and of its targets needs additional in-depth investigations. In particular, future studies are required to better understand the network between USP7 and the E3 ligases complexes that regulate RRM2 to investigate the balance between ubiquitination and deubiquitination across each cell cycle phase.

STAR★METHODS

Detailed methods are provided in the online version of this paper and include the following:

- KEY RESOURCES TABLE
- RESOURCE AVAILABILITY
  - Lead contact
  - Materials availability
  - Data and code availability
- EXPERIMENTAL MODELS AND SUBJECT DETAILS
  - Cell lines and PDXs
  - Mice
- METHOD DETAILS
  - Library
  - *In vivo* shRNA screen
  - Plasmids
  - Lentiviral transfection and infection
  - Cell viability assays, apoptosis and cell cycle analysis
  - Mouse xenograft experiments
  - SA-β-galactosidase tumor section staining, Immunohistochemical staining and scoring
  - RNA preparation and quantitative PCR analysis
  - Senescence-associated β galactosidase (SA-β-gal) activity
  - Senescence-associated secretory phenotype (SASP) analysis
  - Immunofluorescence staining
  - RNA-seq and mass spectrometry (MS)-based proteomic analysis
  - Protein–protein interaction networks functional enrichment analysis
  - Synchronization
  - Protein stability assay
  - Immunoprecipitation and western blot analysis
  - *In vivo* ubiquitination assay and Co-Immunoprecipitation
  - Proximity ligation assay (PLA)
  - Rescue experiments
  - Tissue Microarrays (TMA)
- *IN VITRO* DRUG TREATMENT
- QUANTIFICATION AND STATISTICAL ANALYSIS

SUPPLEMENTAL INFORMATION

Supplemental information can be found online at https://doi.org/10.1016/j.celrep.2022.111396.

ACKNOWLEDGMENTS

The authors thank C. Nino for helpful suggestions, continuous support and discussions, and critical reading of the manuscript and S. Averaimo for revision and correction of the manuscript. We also thank P.P. Di Fiore and the Molecular Pathology Unit of the European Institute of Oncology for providing and screening the TMA, A. Gobbi and M. Capillo for excellent support of animal work, S. Rodighiero and C. Soriani for help with image evaluation, and E. Mileti for SA-β-gal staining of tumor sections. We also thank BioRender, with which we created the graphical abstract. This work was supported by a FUV fellowship and partially supported by AIRC grant IG 2017 Id 20508 (to L.L.) and the Italian Ministry of Health with Ricerca Corrente and 5x1000 funds.

AUTHOR CONTRIBUTIONS

L.G. and L.L. conceived the experimental design. L.G., F.M., M.M., D.B., T.B., S.C., and G.B. developed the methodology. P.N., F.P., G.G., N.M., and A.C. managed experimental assays. L.G., F.M., G.B., M.M., and L.L. analyzed and interpreted the data. L.L. supervised the research. L.G. and L.L. wrote the manuscript.

DECLARATION OF INTERESTS

The authors declare no competing interests.

Received: September 23, 2021
Revised: July 1, 2022
Accepted: August 31, 2022
Published: September 20, 2022

REFERENCES

Aird, K.M., Zhang, G., Li, H., Tu, Z., Bitler, B.G., Garipov, A., Wu, H., Wei, Z., Wagner, S.N., Herlyn, M., and Zhang, R. (2013). Suppression of nucleotide metabolism underlies the establishment and maintenance of oncogene-induced senescence. Cell Rep. *3*, 1252–1265.

Aladowicz, E., Granieri, L., Marocchi, F., Punzi, S., Giardina, G., Ferrucci, P.F., Mazzarol, G., Capra, M., Viale, G., Confalonieri, S., et al. (2020). Shcd binds Dock4, promotes ameboid motility and metastasis dissemination, predicting poor prognosis in melanoma. Cancers (Basel) *12*, 3366.

Alam, M.S. (2018). Proximity ligation assay (Pla). Curr. Protoc. Immunol. *123*, e58.

Anders, S., and Huber, W. (2010). Differential expression analysis for sequence count data. Genome Biol. *11*, R106.

Anders, S., Pyl, P.T., and Huber, W. (2015). Htseq–A Python framework to work with high-throughput sequencing data. Bioinformatics *31*, 166–169.

Bandyopadhyay, D., Curry, J.L., Lin, Q., Richards, H.W., Chen, D., Hornsby, P.J., Timchenko, N.A., and Medrano, E.E. (2007). Dynamic assembly of chromatin complexes during cellular senescence: implications for the growth arrest of human melanocytic nevi. Aging Cell *6*, 577–591.

Bhattacharya, S., Chakraborty, D., Basu, M., and Ghosh, M.K. (2018). Emerging insights into hausp (Usp7) in Physiology, cancer and other diseases. Signal Transduct. Target. Ther. *3*, 17.

Bielak-Zmijewska, A., Mosieniak, G., and Sikora, E. (2018). Is dna damage indispensable for stress-induced senescence? Mech. Ageing Dev. *170*, 13–21.

Bossi, D., Cicalese, A., Dellino, G.I., Luzi, L., Riva, L., D'alesio, C., Diaferia, G.R., Carugo, A., Cavallaro, E., Piccioni, R., et al. (2016). Vivo genetic screens of patient-derived tumors revealed unexpected frailty of the transformed phenotype. Cancer Discov. *6*, 650–663.

Bremm, A., Freund, S.M.V., and Komander, D. (2010). Lys11-Linked ubiquitin chains adopt compact conformations and are preferentially hydrolyzed by the deubiquitinase cezanne. Nat. Struct. Mol. Biol. *17*, 939–947.

Chabes, A.L., Pfleger, C.M., Kirschner, M.W., and Thelander, L. (2003). Mouse ribonucleotide reductase R2 protein: a new target for anaphase-promoting complex-cdh1-mediated proteolysis. Proc. Natl. Acad. Sci. USA *100*, 3925–3929.

Chabes, A.L., Björklund, S., and Thelander, L. (2004). S phase-specific transcription of the mouse ribonucleotide reductase R2 gene requires both A proximal repressive e2f-binding site and an upstream promoter activating region. J. Biol. Chem. *279*, 10796–10807.

Chen, S., Liu, Y., and Zhou, H. (2021). Advances in the development ubiquitin-specific Peptidase (usp) inhibitors. Int. J. Mol. Sci. *22*, 4546.

Cox, J., Hein, M.Y., Luber, C.A., Paron, I., Nagaraj, N., and Mann, M. (2014). Accurate proteome-wide label-free quantification by delayed normalization and maximal peptide ratio extraction, termed maxlfq. Mol. Cell. Proteomics *13*, 2513–2526.

D'angiolella, V., Donato, V., Forrester, F.M., Jeong, Y.T., Pellacani, C., Kudo, Y., Saraf, A., Florens, L., Washburn, M.P., and Pagano, M. (2012). Cyclin F-mediated degradation of ribonucleotide reductase M2 controls genome integrity and dna repair. Cell *149*, 1023–1034.

D'arcy, P., Wang, X., and Linder, S. (2015). Deubiquitinase inhibition as A cancer therapeutic strategy. Pharmacol. Ther. *147*, 32–54.

Damsky, W., Micevic, G., Meeth, K., Muthusamy, V., Curley, D.P., Santhanakrishnan, M., Erdelyi, I., Platt, J.T., Huang, L., Theodosakis, N., et al. (2015). Mtorc1 activation blocks brafv600e-induced growth arrest but is insufficient for melanoma formation. Cancer Cell *27*, 41–56.

Degregori, J., Kowalik, T., and Nevins, J.R. (1995). Cellular targets for activation by the E2f1 transcription factor include dna synthesis- and G1/S-regulatory genes. Mol. Cell Biol. *15*, 4215–4224.

Demaria, M., O'leary, M.N., Chang, J., Shao, L., Liu, S., Alimirah, F., Koenig, K., Le, C., Mitin, N., Deal, A.M., et al. (2017). Cellular senescence promotes adverse effects of chemotherapy and cancer relapse. Cancer Discov. *7*, 165–176.

Enge, M., Bao, W., Hedström, E., Jackson, S.P., Moumen, A., and Selivanova, G. (2009). Mdm2-Dependent downregulation of P21 and hnrnp K provides A switch between apoptosis and growth arrest induced by pharmacologically activated P53. Cancer Cell *15*, 171–183.

Fatkhutdinov, N., Sproesser, K., Krepler, C., Liu, Q., Brafford, P.A., Herlyn, M., Aird, K.M., and Zhang, R. (2016). Targeting Rrm2 and mutant braf is A novel combinatorial strategy for melanoma. Mol. Cancer Res. *14*, 767–775.

Galarreta, A., Lecona, E., Valledor, P., Ubieto, P., Lafarga, V., Specks, J., and Fernandez-Capetillo, O. (2018). Usp7 couples dna replication termination to mitotic entry. Preprint at bioRxiv, 305318. https://doi.org/10.1101/305318.

Gao, L., Zhu, D., Wang, Q., Bao, Z., Yin, S., Qiang, H., Wieland, H., Zhang, J., Teichmann, A., and Jia, J. (2021). Proteome analysis of Usp7 substrates revealed its role in melanoma through Pi3k/akt/foxo and ampk pathways. Front. Oncol. *11*, 736438.

Garzón, J., Rodríguez, R., Kong, Z., Chabes, A., Rodríguez-Acebes, S., Méndez, J., Moreno, S., and García-Higuera, I. (2017). Shortage of dntps underlies altered replication dynamics and dna breakage in the absence of the apc/C cofactor Cdh1. Oncogene *36*, 5808–5818.

Giovinazzi, S., Morozov, V.M., Summers, M.K., Reinhold, W.C., and Ishov, A.M. (2013). Usp7 and daxx regulate mitosis progression and taxane sensitivity by affecting stability of aurora-A kinase. Cell Death Differ. *20*, 721–731.

Guo, J., Zhang, J., Liang, L., Liu, N., Qi, M., Zhao, S., Su, J., Liu, J., Peng, C., Chen, X., and Liu, H. (2020). Potent usp10/13 antagonist spautin-1 suppresses melanoma growth via ros-mediated dna damage and exhibits synergy with cisplatin. J. Cell Mol. Med. *24*, 4324–4340.

Hanahan, D., and Weinberg, R.A. (2000). The hallmarks of cancer. Cell *100*, 57–70.

Hanahan, D., and Weinberg, R.A. (2011). Hallmarks of cancer: the next generation. Cell *144*, 646–674.

He, Y., Li, W., Lv, D., Zhang, X., Zhang, X., Ortiz, Y.T., Budamagunta, V., Campisi, J., Zheng, G., and Zhou, D. (2020). Inhibition of Usp7 activity selectively eliminates senescent cells in Part Via restoration of P53 activity. Aging Cell *19*, E13117.

Huang, X., and Dixit, V.M. (2016). Drugging the undruggables: exploring the ubiquitin system for drug development. Cell Res. *26*, 484–498.

Huang, D.W., Sherman, B.T., Tan, Q., Collins, J.R., Alvord, W.G., Roayaei, J., Stephens, R., Baseler, M.W., Lane, H.C., and Lempicki, R.A. (2007). The david gene functional classification tool: a novel biological module-centric algorithm to functionally analyze large gene lists. Genome Biol. *8*, R183.

Inui, K., Zhao, Z., Yuan, J., Jayaprakash, S., Le, L.T.M., Drakulic, S., Sander, B., and Golas, M.M. (2017). Stepwise assembly of functional C-terminal rest/nrsf transcriptional repressor complexes as a drug target. Protein Sci. *26*, 997–1011.

Kategaya, L., Di Lello, P., Rougé, L., Pastor, R., Clark, K.R., Drummond, J., Kleinheinz, T., Lin, E., Upton, J.P., Prakash, S., et al. (2017). Usp7 small-molecule inhibitors interfere with ubiquitin binding. Nature *550*, 534–538.

Kim, D., Pertea, G., Trapnell, C., Pimentel, H., Kelley, R., and Salzberg, S.L. (2013). Tophat2: accurate alignment of transcriptomes in the presence of insertions, deletions and gene fusions. Genome Biol. *14*, R36.

Lecona, E., Rodriguez-Acebes, S., Specks, J., Lopez-Contreras, A.J., Ruppen, I., Murga, M., Muñoz, J., Mendez, J., and Fernandez-Capetillo, O. (2016). Usp7 is A sumo deubiquitinase essential for dna replication. Nat. Struct. Mol. Biol. *23*, 270–277.

Li, Y., and Reverter, D. (2021). Molecular mechanisms of DUBs regulation in signaling and disease. Int. J Mol. Sci. *22*, 986.

Lian, C.G., Fang, R., Zhan, Q., Ma, J., Lee, C., Frank, M.H., Shi, Y.G., and Murphy, G.F. (2013). Inhibition of lysine-specific histone demethylase Lsd1 suppresses melanoma growth. FASEB J. *27*, 1088.

Luise, C., Capra, M., Donzelli, M., Mazzarol, G., Jodice, M.G., Nuciforo, P., Viale, G., Di Fiore, P.P., and Confalonieri, S. (2011). An atlas of altered expression of deubiquitinating enzymes in human cancer. PLoS One *6*, E15891.

Mannava, S., Moparthy, K.C., Wheeler, L.J., Natarajan, V., Zucker, S.N., Fink, E.E., Im, M., Flanagan, S., Burhans, W.C., Zeitouni, N.C., et al. (2013). Depletion of deoxyribonucleotide pools is an endogenous source of dna damage in cells undergoing oncogene-induced senescence. Am. J. Pathol. *182*, 142–151.

Mazzu, Y.Z., Armenia, J., Chakraborty, G., Yoshikawa, Y., Coggins, S.A., Nandakumar, S., Gerke, T.A., Pomerantz, M.M., Qiu, X., Zhao, H., et al. (2019). A novel mechanism driving poor-prognosis prostate cancer: overexpression of the dna repair gene, ribonucleotide reductase small subunit M2 (Rrm2). Clin. Cancer Res. *25*, 4480–4492.

Minmin, X., Long, L., Xinwei, K., Zuozhong, X., Jing, L., Shuang, Z., Juan, S., Xiang, C., and Hong, L. (2021). Pharmacological inhibition of USP7 suppresses growth and metastasis of melanoma cells in vitro and in vivo. J Cell Mol Med *25*, 9228–9240.

Mungamuri, S.K., Qiao, R.F., Yao, S., Manfredi, J.J., Gu, W., and Aaronson, S.A. (2016). Usp7 enforces heterochromatinization of P53 target promoters by protecting Suv39h1 from mdm2-mediated degradation. Cell Rep. *14*, 2528–2537.

Nakayama, K.I., and Nakayama, K. (2006). Ubiquitin ligases: cell-cycle control and cancer. Nat. Rev. Cancer *6*, 369–381.

Nijman, S.M.B., Luna-Vargas, M.P.A., Velds, A., Brummelkamp, T.R., Dirac, A.M.G., Sixma, T.K., and Bernards, R. (2005). A genomic and functional inventory of deubiquitinating enzymes. Cell *123*, 773–786.

Nordlund, P., and Reichard, P. (2006). Ribonucleotide reductases. Annu. Rev. Biochem. *75*, 681–706.

Paluvai, H., Di Giorgio, E., and Brancolini, C. (2020). The histone code of senescence. Cells *9*, E466.

Park, J., Cho, J., Kim, E.E., and Song, E.J. (2019). Deubiquitinating Enzymes: A critical regulator of mitosis. Int. J. Mol. Sci. *20*, 5997.

Peng, Y., Liu, Y., Gao, Y., Yuan, B., Qi, X., Fu, Y., Zhu, Q., Cao, T., Zhang, S., Yin, L., and Li, X. (2019). Usp7 is A novel deubiquitinase sustaining Plk1 protein stability and regulating chromosome alignment. J. Exp. Clin. Cancer Res. *38*, 468.

Qin, W., Leonhardt, H., and Spada, F. (2011). Usp7 and Uhrf1 control ubiquitination and stability of the maintenance dna methyltransferase Dnmt1. J. Cell. Biochem. *112*, 439–444.

Rahman, M.A., Amin, A.R.M.R., Wang, D., Koenig, L., Nannapaneni, S., Chen, Z., Wang, Z., Sica, G., Deng, X., Chen, Z.G., and Shin, D.M. (2013). Rrm2 regulates bcl-2 in head and neck and lung cancers: a potential target for cancer therapy. Clin. Cancer Res. *19*, 3416–3428.

Rappsilber, J., Mann, M., and Ishihama, Y. (2007). Protocol for micro-purification, enrichment, pre-fractionation and storage of peptides for proteomics using stagetips. Nat. Protoc. *2*, 1896–1906.

de Sá, B.C.S., Fugimori, M.L., Ribeiro, K.d.C.B., Duprat Neto, J.P., Neves, R.I., Landman, G., Neves, R.I., and Landman, G. (2009). Proteins involved in Prb and P53 pathways are differentially expressed in thin and thick superficial spreading melanomas. Melanoma Res. *19*, 135–141.

Saleh, T., Bloukh, S., Carpenter, V.J., Alwohoush, E., Bakeer, J., Darwish, S., Azab, B., and Gewirtz, D.A. (2020). Therapy-Induced Senescence: An "Old" Friend becomes the enemy. Cancers *12*, 822.

Schneider, C.A., Rasband, W.S., and Eliceiri, K.W. (2012). Nih image to imagej: 25 Years of image analysis. Nat. Methods *9*, 671–675.

Schosserer, M., Grillari, J., and Breitenbach, M. (2017). The dual role of cellular senescence in developing tumors and their response to cancer therapy. Front. Oncol. *7*, 278.

Shen, S., Wolfe, R., Mclean, C.A., Haskett, M., and Kelly, J.W. (2014). Characteristics and associations of high-mitotic-rate melanoma. JAMA Dermatol. *150*, 1048–1055.

Shevchenko, A., Tomas, H., Havlis, J., Olsen, J.V., and Mann, M. (2006). In-gel digestion for mass spectrometric characterization of proteins and proteomes. Nat. Protoc. *1*, 2856–2860.

Siddiqui, M.S., François, M., Fenech, M.F., and Leifert, W.R. (2015). Persistent Gammah2ax: a promising molecular marker of dna damage and aging. Mutat. Res. Rev. Mutat. Res. *766*, 1–19.

Sowa, M.E., Bennett, E.J., Gygi, S.P., and Harper, J.W. (2009). Defining the human deubiquitinating enzyme interaction landscape. Cell *138*, 389–403.

Steger, M., Demichev, V., Backman, M., Ohmayer, U., Ihmor, P., Müller, S., Ralser, M., and Daub, H. (2021). Time-resolved in vivo ubiquitinome profiling by dia-ms reveals Usp7 targets on A proteome-wide scale. Nat. Commun. *12*, 5399.

Subramanian, A., Tamayo, P., Mootha, V.K., Mukherjee, S., Ebert, B.L., Gillette, M.A., Paulovich, A., Pomeroy, S.L., Golub, T.R., Lander, E.S., and Mesirov, J.P. (2005). Gene set enrichment analysis: a knowledge-based approach for interpreting genome-wide expression profiles. Proc. Natl. Acad. Sci. USA *102*, 15545–15550.

Szklarczyk, D., Morris, J.H., Cook, H., Kuhn, M., Wyder, S., Simonovic, M., Santos, A., Doncheva, N.T., Roth, A., Bork, P., et al. (2017). The string database in 2017: quality-controlled protein-protein association networks, made broadly accessible. Nucleic Acids Res. *45*, D362–D368.

Tahara, H., Kamada, K., Sato, E., Tsuyama, N., Kim, J.K., Hara, E., Oda, K., and Ide, T. (1995). Increase in expression levels of interferon-inducible genes in senescent human diploid fibroblasts and in sv40-transformed human fibroblasts with extended lifespan. Oncogene *11*, 1125–1132.

Turnbull, A.P., Ioannidis, S., Krajewski, W.W., Pinto-Fernandez, A., Heride, C., Martin, A.C.L., Tonkin, L.M., Townsend, E.C., Buker, S.M., Lancia, D.R., et al. (2017). Molecular basis of Usp7 inhibition by selective small-molecule inhibitors. Nature *550*, 481–486.

Tyanova, S., Temu, T., and Cox, J. (2016). The maxquant computational platform for mass spectrometry-based shotgun proteomics. Nat. Protoc. *11*, 2301–2319.

Vishnoi, M., Boral, D., Liu, H., Sprouse, M.L., Yin, W., Goswami-Sewell, D., Tetzlaff, M.T., Davies, M.A., Oliva, I.C.G., and Marchetti, D. (2018). Targeting Usp7 identifies A metastasis-competent state within bone marrow-resident melanoma ctcs. Cancer Res. *78*, 5349–5362.

Von Kobbe, C. (2019). Targeting senescent cells: approaches, opportunities, challenges. Aging (Albany NY) *11*, 12844–12861.

Wang, L., Meng, L., Wang, X.W., Ma, G.Y., and Chen, J.H. (2014). Expression of Rrm1 and Rrm2 as A novel prognostic marker in advanced non-small cell lung cancer receiving chemotherapy. Tumour Biol. *35*, 1899–1906.

Wei, Y., Jiang, Z., and Lu, J. (2021). Usp22 promotes melanoma and braf inhibitor resistance via yap stabilization. Oncol. Lett. *21*, 394.

Xiang, M., Liang, L., Kuang, X., Xie, Z., Liu, J., Zhao, S., Su, J., Chen, X., and Liu, H. (2021). Pharmacological inhibition of Usp7 suppresses growth and metastasis of melanoma cells in vitro and in. J. Cell Mol. Med. *25*, 9228–9240.

Xu, W., and Mcarthur, G. (2016). Cell cycle regulation and melanoma. Curr. Oncol. Rep. *18*, 34.

Yeon, M., Kim, Y., Jung, H.S., and Jeoung, D. (2020). Histone deacetylase inhibitors to overcome resistance to targeted and immuno therapy in metastatic melanoma. Front. Cell Dev. Biol. *8*, 486.

Yi, L., Cui, Y., Xu, Q., and Jiang, Y. (2016). Stabilization of Lsd1 By deubiquitinating enzyme Usp7 promotes glioblastoma cell tumorigenesis and metastasis through suppression of the P53 signaling pathway. Oncol. Rep. *36*, 2935–2945.

Yoshida, A., Lee, E.K., and Diehl, J.A. (2016). Induction of therapeutic senescence in vemurafenib-resistant melanoma by extended inhibition of cdk4/6. Cancer Res. *76*, 2990–3002.

Zhao, X., Fiske, B., Kawakami, A., Li, J., and Fisher, D.E. (2011). Regulation of mitf stability by the Usp13 deubiquitinase. Nat. Commun. *2*, 414.

Zhou, J., Wang, J., Chen, C., Yuan, H., Wen, X., and Sun, H. (2018). Usp7: target validation and drug discovery for cancer therapy. Med. Chem. *14*, 3–18.

Zhu, Q., Sharma, N., He, J., Wani, G., and Wani, A.A. (2015). Usp7 deubiquitinase promotes ubiquitin-dependent dna damage signaling by stabilizing Rnf168. Cell Cycle *14*, 1413–1425.

Zou, Y., Zhou, J., Xu, B., Li, W., and Wang, Z. (2019). Ribonucleotide reductase subunit M2 as A novel target for clear-cell renal cell carcinoma. Oncotargets Ther. *12*, 3267–3275.

STAR★METHODS

KEY RESOURCES TABLE

REAGENT or RESOURCE	SOURCE	IDENTIFIER
Antibodies		
Rabbit monoclonal anti-HAUSP (clone D17C6) (WB, IF application)	Cell Signaling Technology	Cat#4833; RRID:AB_10557113
Mouse monoclonal anti-USP7 (clone GT6512) (WB application)	Thermo Fisher Scientific	Cat#MA5-31516; RRID:AB_2787147
Rabbit polyclonal anti-HAUSP (IHC application)	Abcam	Cat#ab4080, RRID:AB_2214019
Rabbit polyclonal anti-RRM2 (WB, IF application)	GeneTex	Cat#GTX33480; RRID:N/A
Mouse monoclonal anti-RRM2 (IHC application)	Abcam	Cat#ab57653, RRID:AB_2253869
Mouse monoclonal anti-p21 (clone F-5)	Santa Cruz Biotechnology	Cat#sc-6246, RRID:AB_628073
Rabbit polyclonal anti-PARP	Cell Signaling Technology	Cat#9542, RRID:AB_2160739
Rabbit polyclonal anti-LMNB1	Abcam	Cat#ab16048, RRID:AB_443298
Rabbit monoclonal anti-Rb (Phospho Ser807/811) (clone D20B12)	Cell Signaling Technology	Cat#8516, RRID:AB_11178658
Mouse monoclonal anti-TP53 (clone DO-1)	Santa Cruz Biotechnology	Cat#sc-126, RRID:AB_628082
Mouse monoclonal anti-MDM2 (clone SMP14)	Santa Cruz Biotechnology	Cat#sc-965, RRID:AB_627920
Rabbit polyclonal anti-MTOR (Phospho-Ser2448)	Elabscience	Cat#E-AB-20929 RRID:N/A
Rabbit polyclonal anti-p70 S6 kinase (Phospho-Thr421/Ser424)	Cell Signaling Technology	Cat#9204, RRID:AB_2265913
Rabbit polyclonal anti-S6 Ribosomal Protein (Phospho-Ser235/236)	Cell Signaling Technology	Cat#2211, RRID:AB_331679
Mouse monoclonal anti-H2A.X (Phospho-Ser139)	BioLegend	Cat#613402, RRID:AB_315795
Rabbit polyclonal anti-Cleaved Caspase-3 (Asp175)	Cell Signaling Technology	Cat#9661, RRID:AB_2341188
Rabbit polyclonal anti-P16 (clone N-20)	Santa Cruz Biotechnology	Cat#sc-467, RRID:AB_632101
Mouse monoclonal anti-Ubiquitin (clone P4D1)	Santa Cruz Biotechnology	Cat#sc-8017, RRID:AB_628423
Rabbit polyclonal anti-Anillin	Thermo Fisher Scientific	Cat#PA5-114851, RRID:AB_2899487
Rabbit polyclonal anti-KIF11	Thermo Fisher Scientific	Cat#PA5-115164, RRID:AB_2899800
Rabbit polyclonal anti-HDAC1	Abcam	Cat#ab7028, RRID:AB_305705
Rabbit polyclonal anti-HDAC2	Abcam	Cat#ab7029, RRID:AB_305706
Mouse monoclonal anti-HDAC3 (clone 3G6)	Millipore	Cat#05-813, RRID:AB_11213594
Rabbit polyclonal anti-acetyl-Histone H3	Millipore	Cat#06-599, RRID:AB_2115283
Mouse monoclonal anti-H3 (1G1)	Santa Cruz Biotechnology	Cat#sc-517576, RRID:AB_2848194
Rabbit monoclonal anti-GAPDH (clone 14C10)	Cell Signaling Technology	Cat#2118, RRID:AB_561053
Mouse monoclonal anti-Vinculin (Clone hVIN-1)	Sigma-Aldrich	Cat#V9131, RRID:AB_477629
Mouse monoclonal anti-p21, FITC Conjugated, (Clone 26)	BD Biosciences	Cat#612236, RRID:AB_399559
Rabbit polyclonal anti-Ki-67, PE Conjugated	Bioss	Cat#bs-2130R-PE, RRID:AB_11055106
Mouse monoclonal anti-BrdU	BD Biosciences	Cat#347580, RRID:AB_10015219
Rabbit polyclonal anti-Alexa Fluor 488 (H+L)	Jackson ImmunoResearch Labs https://www.thermofisher.com/fr/en/home/brands/invitrogen.html	Cat#715-545-150, RRID:AB_2340846
Bacterial and virus strains		
Stbl3 competent cells	Life Technologies	Cat#C737303

(*Continued on next page*)

Continued

REAGENT or RESOURCE	SOURCE	IDENTIFIER
Chemicals, peptides, and recombinant proteins		
P005091 (P5091, USP7 inhibitor)	APExBIO	Cat#A3023; CAS: 882257-11-6
GNE-6640 (USP7 inhibitor)	MedChemExpress, MCE	Cat#HY-112937; CAS: 2009273-67-8
CF3-FT671 (USP7 inhibitor)	AOBIUS	Cat#AOB36638; CAS: 1959551-26-8
Domatinostat (4SC-202, HDAC inhibitor)	Selleck Chemicals	Cat#S7555; CAS: 910462-43-0
Vorinostat	Selleck Chemicals	Cat#S1047; CAS: 149647-78-9
Belinostat (HDAC inhibitor)	MedChemExpress, MCE	Cat#HY-10225; CAS 866323-14-0
5-Bromo-2′-deoxyuridine (BrdU)	Sigma-Aldrich	Cat#B5002; CAS: 59-14-3
5-Bromo-4-Chloro-3-Indolyl-β-D-Galactopyranoside (X-gal)	Inalco	Cat#17580300; CAS: 7240-90-6
Dimethyl sulfoxide (DMSO)	Sigma-Aldrich	Cat#D1435; CAS:67-68-5
Puromycin	VINCI-BIOCHEM	Cat#AG-CN2-0078
Blasticidin	Gibco	Cat#R210-01; CAS:2079-00-7
Propidium Iodide Solution	Sigma-Aldrich	Cat#P4864
RNAaseA	Sigma-Aldrich	Cat#10109169001
4′,6-diamidino-2-phenylindole (DAPI)	Sigma-Aldrich	Cat#32670
Tween80	Sigma-Aldrich	Cat#P1754
Poly (ethylene glycol) PEG300	Sigma-Aldrich	Cat#202371
Glutaraldehyde	Sigma-Aldrich	Cat#340855
Thymidine	Sigma-Aldrich	Cat#T1895
Cycloheximide (CHX)	Sigma-Aldrich	Cat#C7698
MG132	Sigma-Aldrich	Cat#474790
PR-619 (UPS inhibitor)	TebuBio	Cat#SI9619
Polybrene	Sigma-Aldrich	Cat#638132; CAS: 28728-55-4
Paraformaldehyde 4%	ChemCruz	Cat#sc-281692
Triton-X-100	Prolabo	Cat#28817-295
Iscove′s Modified Dulbecco′s Medium (IMDM)	Sigma-Aldrich	Cat#I3390
HyClone™ Fetal Bovine Serum (North U.S.)	HyClone products Cytiva	Cat#SH30071.03IH
Trypsin	EuroClone	Cat#ECB3052D
l-Glutamine	EuroClone	Cat#ECB3000D
Penicillin/ Streptomycin	EuroClone	Cat#ECB3001D
L15	Sigma-Aldrich	Cat#L5520
Matrigel Matrix HC	Corning	Cat#354248
Bovine Serum Albumin	Cabru	Cat#033IDB1000-70-1
Not-fat dried Milk powder	AppliChem	Cat#A0830
Protein A Sepharose CL-4B beads	GE-Healthcare	Cat#GE17-0780-01
NuPAGE® Novex 4-12% gradient gels	Thermo Fisher Scientific	Cat#NP0321
Protease inhibitor cocktail	Roche	Cat#11697498001
Phosphatase inhibitor cocktail	ThermoScientific	Cat#A32957
AMPure XP beads	Beckman Coulter	Cat# A63881
DPBS1X	MICROGEM	Cat#TL1006
Mowiol	Merk Life Science	Cat#81838
Hematoxylin Solution, Harris Modified	Sigma-Aldrich	Cat#HHS80; CAS: N/A
Eukitt	Bio-Optica	Cat#09-09251
Eosin Y-solution 0.5% aqueous	Sigma-Aldrich	Cat#109844; CAS: N/A
Polyvinyl alcohol mounting medium with DABCO	Merk Life Science	Cat#10981; CAS: N/A
Fast Sybr Green Master Mix	Applied Biosystem	Cat#4385614

(*Continued on next page*)

Continued

REAGENT or RESOURCE	SOURCE	IDENTIFIER
Critical commercial assays		
CellTiter-Glo® Luminescent Cell Viability Assay	Promega	Cat#G7570
Caspase Glo 3-7 assay	Promega	Cat#G8093
CyQuant™ Direct Cell Proliferation Assay	Thermo Fisher Scientific	Cat#C35012
Cell Tox™ Green Cytotoxicity Assay	Promega	Cat# G8741
DAB Substrate Kit, Peroxidase (HRP), with Nickel, (3,3'-diaminobenzidine)	Vector Laboratories	SK-4100; CAS: N/A
Quick-RNA MiniPrep	Zymo Research	Cat#R1055
OneScript Plus cDNA synthesis kit	Abm	Cat#G236
Cellular Senescence Detection Kit - SPiDER-ßGal	Dojindo	Cat#SG03
Human Premixed Multi-Analyte kit	R&D Systems by Bio-Techne	Cat#LXSAHM-04, Cat#LXSAHM-21, Cat#LXSAHM-29
TruSeq RNA Library Preparation Kit v2	Illumina	Cat#15025063
BCA Protein Assay Kit	Pierce	Cat#23225
Protein Assay Dye Reagent Concentrate	Bio-Rad	Cat#500-0006
Proximity Ligation Assay kit	Duolink, Sigma-Aldrich	Cat#DUO92004
Deposited data		
Raw RNA seq Data	This study	GEO: GSE180986
Raw Mass Spec Data	This study	PRIDE: PXD034260; ID#589847
Experimental models: Cell lines		
MM27 (Metastatic melanoma Patient Derived Xenograft, male)	This study	N/A
MM13 (Metastatic melanoma Patient Derived Xenograft, male)	This study	N/A
MM25 (Metastatic melanoma Patient Derived Xenograft, female)	This study	N/A
MM16 (Metastatic melanoma Patient Derived Xenograft, male)	This study	N/A
A-375 (Human Skin, Malignant melanoma Cell Line)	IZSBS	CRL1619; RRID:CVCL_0132
HEK-293T (Human Embryonic kidney cell line)	ATCC	CRL-3216; RRID:CVCL_0063
Experimental models: Organisms/strains		
NOD.Cg-Prkdc^{scid} Il2rg^{tm1Wjl}/SzJ (termed NSG) male and female mice	Charles River	NSG-HLA-A2/HHD (014570)
Oligonucleotides		
shRNA targeting sequence: shScr#1 (5′-3′) AAAGGCGGTATCGGTAAATT TGTTAATATTCATAGCAGATTTACC GATACCGCCTTT	This study	N/A
shRNA targeting sequence: shScr#2 (5′-3′) AACAACCGTGATCTGTGTGA TGTTAATATTCATAGCATCACGCAG ATCGCGGTTGTT	This study	N/A
shRNA targeting sequence: shUSP7#154 (5′-3′) CCGGCCAGCTAAGTATCAAAG GAAACTCGAGTTTCCTTTGATACTTA GCTGGTTTTTG	This study	N/A
shRNA targeting sequence: shUSP7156#2 (5′-3′) CCGGCGTGGTGTCAAGGTGTAC TAACTCGAGTTAGTACACCTTGACA CCACGTTTTTG	This study	N/A

(*Continued on next page*)

Continued

REAGENT or RESOURCE	SOURCE	IDENTIFIER
shRNA targeting sequence: shp21#1 GGTGACTTCGCCTGGGAGCGTCTCGAG ACGCTCCCAGGCGAAGTCACC	This study	N/A
shRNA targeting sequence: shp21#2 GTCACTGTCTTGTACCCTTGT CTCGAGACAAGGGTACAAGACAGTGAC	This study	N/A
shRNA targeting sequence: shRRM2#1, GCTCAAGAAACGAGGACTGAT	This study	N/A
shRNA targeting sequence: shRRM2#2 GCAGACAGACTTATGCTGGAA	This study	N/A
Primer for qPCR, human USP7 forward (5′-3′), GATGAAAAGTCGTTCAGTCGTCG	This study	N/A
Primer for qPCR, human USP7 reverse (5′-3′), TTTGAATCCCACGCAACTCCA	This study	N/A
Primer for qPCR, human RPLP0 forward (5′-3′), TTCATTGTGGGAGCAGAC	This study	N/A
Primer for qPCR, human RPLP0 reverse (5′-3′), CAGCAGTTTCTCCAGAGC	This study	N/A
Primer for qPCR, human DNAJC9 forward (5′-3′), AACAGTGGACGAGGACTCTCCT	This study	N/A
Primer for qPCR, human DNAJC9 reverse (5′-3′), AGCCAGCTCTTCTTCCGAACCT	This study	N/A
Primer for qPCR, human UBE2V2 forward (5′-3′), AAGGAGTAGGCGACGGTACA	This study	N/A
Primer for qPCR, human UBE2V2 reverse (5′-3′), ACGGAGGAGCTTCTGGGTAT	This study	N/A
Primer for qPCR, human ELL2 forward (5′-3′), TGACTGCATCCAGCAAACAT	This study	N/A
Primer for qPCR, human ELL2 reverse (5′-3′), TCGTTTGTTGCACACACTGTAA	This study	N/A
Primer for qPCR, human CCNA2	Thermofisher	Cat#Hs00153138
Primer for qPCR, human CCNB1	Thermofisher	Cat#Hs00259126
Primer for qPCR, human CCND1	Thermofisher	Cat#Hs00277039
Primer for qPCR, human CCNE2	Thermofisher	Cat#Hs00372959
Recombinant DNA		
pRSI-U6-(sh)-UbiC- GFP-2A-Puro lentiviral vector (shRNA Library), custom made	Cellecta	CPLVSHL-1K4-O CPLVSHL-1K4-P CLVP-5E
MISSION lentiviral pLKO.1 shRRM2	Sigma-Aldrich	Cat#SHCLNG
Empty Control Vector (pLX304-CMV-Blast -V5)	DNASu plasmid Repository	Cat#EvNO00877063
RRM2 Overexpressing Vector (pLX304-CMV-RRM2-Blast-V5)	DNASu plasmid Repository	Cat#HsCD00445387
pLKO.1-U6-(sh)-Puro lentiviral vector	Sigma-Aldrich	Cat#SHC001
Software and algorithms		
FlowJo Software V10.7.2	BD Biosciences	https://www.flowjo.com
ImageJ	Schneider et al., 2012	https://imagej.nih.gov/ij/
GraphPad Prism 9.0	GraphPad Software	https://www.graphpad.com/scientific/software/prism
TopHat2 2.0.9	Kim et al., 2013	https://ccb.jhu.edu/software/tophat/
Bioconductor-DESeq (1.30.0) R package	Anders and Huber, 2010	ease/bioc/html/DESeq.html
DAVID tool Version 6.8 Beta	Huang et al., 2007	https://david.ncifcrf.gov
Ingenuity Pathway Analysis (IPA)	Qiagen	www.ingenuity.com

(*Continued on next page*)

Continued

REAGENT or RESOURCE	SOURCE	IDENTIFIER
Gene Set Enrichment Analysis (GSEA) software v2.2.0	Subramanian et al., 2005	http://software.broadinstitute.org/gsea/
MaxQuant software (version 1.6.2.3)	Tyanova et al., 2016	https://www.maxquant.org
STRING v11.0	Szklarczyk et al., 2017	https://string-db.org
JMP 14.0 statistical software	JMP	https://www.jmp.com
LASX Acquisition Software	Leica	N/A
Biorender software	BioRender	https://app.biorender.com
Other		
FACS Celesta BD	Bioscience	N/A
Aperio ScanScope system	Leica Biosystems	N/A
CFX-96	Biorad	N/A
BioAnalyzer	Agilent 2100	N/A
HiSeq™-2000	Illumina	N/A
Leica histo-fluo microscope	Leica Biosystems	N/A
Luminex 200 System xMap Thecnology	BioRad	N/A
EASY-nLC 1200	Thermo Fisher Scientific	N/A
Evos microscope	Evos	N/A
Leica DM6B fluorescence microscope	Leica Biosystems	N/A
NanoDrop ND-1000	EuroClone	N/A

RESOURCE AVAILABILITY

Lead contact

Further information and requests for resources and reagents should be directed to and will be fulfilled by the lead contact, Luisa Lanfrancone (luisa.lanfrancone@ieo.it).

Materials availability

All plasmids and cell lines generated in this study are available from the lead contact upon request with a completed Material Transfer Agreement.

Data and code availability

- RNA-seq and Mass Spec data have been deposited at GEO and PRIDE respectively and are publicly available. Accession numbers are listed in the key resources table.
- This paper does not report original code.
- Any additional information required to reanalyze the data reported in this paper is available from the lead contact upon request.

EXPERIMENTAL MODELS AND SUBJECT DETAILS

Cell lines and PDXs

A375 (Human malignant melanoma cell line) and HEK-293T (Human Embryonic kidney cell line) were maintained in Dulbecco's modified Eagle's medium (DMEM) supplemented with 10% South American origin FBS, 200 mmol/L glutamine, 100 U/mL penicillin and 100 g/mL streptomycin.

Melanoma metastatic PDXs, MM27, MM13, MM25, MM16 were obtained and maintained in culture in Iscove's modified Dulbecco's medium (IMDM) supplemented with 200 mmol/L L-glutamine and 10% FBS.

Mice

PDX were generated in NOD.Cg-Prkdcscid Il2rgtm1Wjl/SzJ (NSG) mice as previously described (Bossi et al., 2016). Briefly, tissue biopsies of metastatic melanomas were collected from patients whose informed consent was obtained in writing according to the policies of the Ethics Committee of the European Institute of Oncology and regulations of the Italian Ministry of Health. The studies were conducted in full compliance with the Declaration of Helsinki. Tumors were mechanically dissociated and subsequently digested with an enzymatic combination of Collagenase Type III (1 mg/mL, Worthington Biochem) and Dispase (0.5 U/mL, STEMCELL-Technologies) for 45 min at 37°C. After incubation, cells were treated with red blood cell lysis buffer (155 mmol/L

NH4Cl, 12 mmol/L NaHCO3, 0.1 mmol/L EDTA) to remove erythrocytes, and then filtered (40-μm cell strainer) to obtain a single-cell suspension. To generate primary PDX1s, 100,000–500,000 dissociated cells were resuspended in a 3:1 mix of L15 medium and Matrigel Matrix and subcutaneously injected into the flank of NSG mice. Tumor formation was monitored weekly, and tumor diameters measured with calipers. Mice were sacrificed when tumors reached the volume of ~0.5 cm^3. PDX1 tumors were dissociated as patient biopsies, and either serially transplanted to obtain secondary and tertiary PDXs (PDX2s and PDX3s) or snap-frozen. Purity of PDX-dissociated human melanoma cells (≥95%) was evaluated, analyzing HLA (BD555555) expression by FACS Aria.

In vivo studies were performed after approval from our fully authorized animal facility and notification to the Ministry of Health (as required by the Italian Law; IACUCs No 02/2012 and No 758/2015-PR), and in accordance with EU directive 2010/63. Both females and males mice were used at the age of 7–8 weeks.

METHOD DETAILS

Library

The human shRNA library was purchased by Cellecta (Cellecta Inc.) and engineered into the pRSI-U6-(sh)-UbiC- GFP-2A-Puro lentiviral vector, as previously described (Bossi et al., 2016). The library contains 2894 vectors, targeting 289 genes (10 different shRNAs per gene), two positive controls (PSMA1, 10 shRNA/gene; RPL30, 4 shRNA/gene) and one neutral control (LUC, 16 shRNA/gene). Targeting genes belong to the Ubiquitin Proteasome System (UPS), Helicases (HELs) and cell metabolism-related genes (CM).

In vivo shRNA screen

The *in vivo* shRNA screen was performed as reported (Bossi et al., 2016). Briefly, PDX cells (MM27, MM13) at passage two were infected with the shRNA library at low Multiplicity Of Infection (MOI~ 0.1-0.5) and puromycin selected. Transduced cells were used as reference, while 330,000 cells *per* mouse (400 cells/BC) were subcutaneously (s.c.) injected in NSG mice. Genomic DNA extraction, library BCs amplification and sequencing, and screen analysis were performed as previously reported (Bossi et al., 2016).

Plasmids

The shRNAs were cloned into the pLKO.1-U6-(sh)-Puro lentiviral vector (Sigma-Aldrich, SHC001). Control vectors carry scrambled non-targeting shRNAs (shScr#1, shScr#2), while 2 shUSP7 and 2 shp21 vectors were generated (shUSP7#154, shUSP7156; shp21#1, shp21#2). MISSION lentiviral pLKO.1 constructs containing RRM2 shRNAs were purchased from Sigma-Aldrich (shRRM2#1, shRRM2#2).

For RRM2 overexpression, the empty vector pLX304-CMV-Blast -V5 and pLX304 -CMV-RRM2-Blast-V5 were purchased from DNASu plasmid Repository.

Lentiviral transfection and infection

The HEK-293T packaging cells were transfected using the calcium phosphate method, as previously described (Bossi et al., 2016). Lentiviral particles from single plasmids were produced and viral titer was calculated in A375 melanoma cell line. Either single shRNA (sh154, sh156) or shRNA pools were added to PDXs cultures at MOI~3 or ~5 for 16 h in standard medium supplemented with 4 μg/mL polybrene, followed by complete medium replacement. Puromycin (2 μg/mL) or Blasticidin (3 μg/mL) was added 48 h post-infection and surviving cells harvested after 3 days or 5 days respectively.

Cell viability assays, apoptosis and cell cycle analysis

Five days post-infection, PDX cells were plated in triplicate in 96 well plates (1.5×10^3/well). Cell proliferation was measured at different time points by CellTiter-Glo assay and apoptosis was detected by Caspase Glo 3-7 assay, as described in the manufacturer's protocol.

1.5×10^6 cells were seeded in 10 cm plates and the day after cell cycle distribution was monitored by BrdU (Bromodeoxyuridine) incorporation. Cells were pulsed for 1h with 33 μM BrdU, then harvested and fixed in 70% of ethanol. Cells were denaturated with 2 M HCl for 25′ and the reaction was stopped adding Sodium Borate pH 8.5 for 2'. Cells were stained with anti-BrdU and FITC secondary antibodies and resuspended in staining solution with propidium iodide (PI) and RNaseA. Stained cells were analyzed by fluorescent-activated cell sorting (FACS). Analysis was performed using FlowJo analysis software and comparisons between two groups were assessed by using two-tailed unpaired Student's t test (Ttest).

Mouse xenograft experiments

For shUSP7 *in vivo* studies, 2.5×10^5 MM27, MM13, MM25, MM16 PDX cells at passage two were transduced with control shRNA (shScr) or pooled shUSP7 (#shUSP7-154 and #shUSP7-156, 5 or 6 mice *per* group) and then subcutaneously transplanted into the right flank of NSG mice with 1:3 Matrigel Matrix HC and L15 medium. Tumor growth was monitored every 3 days in two dimensions using a digital caliper and sacrificed when the tumor reached ~0.8 cm^3 in volume (V), or before this maximum volume allowed in case of ulcers conditions. Tumor volumes were calculated using the modified ellipsoid formula $V = L \times l^2/2$ (L length; l width). The statistical difference in tumor volume among the two groups was assessed by Student's *t-test*. Survival analysis was calculated with GraphPad Prism 9.0, and differences among groups were estimated by using Log rank test.

For the analysis of drug responses *in vivo*, 2.5×10^5 MM27 cells were injected as reported above. Tumors were allowed to grow for about 10 days, followed by exclusion of outliers, randomization of the experimental groups and start of treatment.

For the single P5091 treatment, 7 mice per group were treated intravenously with either vehicle or 15 mg/kg P5091 (4% DMSO and 4% Tween80) twice a week for 3 weeks. Mice were constantly monitored, checked in body weight and tumor growth as described above.

For the P5091 and domatinostat combination treatment, the four mice groups (Ctr = 7, P5091 = 8, domatinostat = 7, P5091 + domatinostat = 7) were treated when tumors reached around 80 mm^3 with the following treatment scheme: twice per week intravenous treatment for P5091 (15mg/kg) and daily oral gavage with domatinostat (60 mg/kg) for 5 days, followed by two days off. The treatment scheme was repeated for a total of 3 weeks. Domatinostat was dissolved in 2% DMSO, 30% PEG300, 5% Tween80. Mice were constantly monitored in tumor size and body weight as previously described.

SA-β-galactosidase tumor section staining, Immunohistochemical staining and scoring

Samples were obtained from xenograft tumors MM27 treated or not with P5091 (15 mg/kg), domatinostat (60 mg/kg) or both drug in combination for one week, receiving two intravenous doses of P5091 or/and five oral administrations of domatinostat.

For β-Galactosidase staining, tumor sections were rapidly frozen in liquid nitrogen and mounted in OCT. Thin section were cut (5-10μm), mounted onto glass slides, fixed in COLD slide fixative (0.2% Glutaraldehyde) for 10 min, washed in DPBS1X and immersed at 37°C for 16 h in homemade SA-β-Gal staining solution (1 mg/mL 5-bromo-4-chloro-3-indolyl-beta-d-galactopyranoside (X-gal), 40 mM citric acid, 160 mM Na_2HPO_4, 30 mM NaH_2PO_4, 5 mM potassium ferricyanide, 5 mM potassium ferrocyanide, 150 mM NaCl, and 2 mM $MgCl_2$, 5% DMSO, pH = 6). Sections were then counterstained with eosin, mounted in Mowiol-DABCO and viewed under Leica histo-fluo microscope. Individual cells were counted and scored positive (blue) or negative for SA-βGal by using ImageJ tool (Schneider et al., 2012).

For immunoistochemical analysis, tumor sections were formalin-fixed paraffin-embedded. To assess histological features Haematoxylin/Eosin staining was performed according to standard protocols and samples were mounted in Eukitt.

Paraffin was removed with xylene and the sections were rehydrated in graded alcohol. Antigen retrieval was carried out using preheated target retrieval solution for 30 min and endogenous peroxidase activity was quenched with 3% hydrogen peroxide in distilled water for 10 min at RT. Tissue sections were blocked with FBS serum in PBS for 60 min and incubated overnight with primary antibodies. They were probed with the following antibodies: p-(Ser807/811) Rb, RRM2, p21, Lamin B1, γ-(P-Ser139) H2AX and Cleaved Caspase-3.

The antibody binding was detected using a polymer detection kit followed by a diaminobenzidine chromogen reaction. All sections were counterstained with Mayer's hematoxylin.

The whole slides and pictures were acquired with the Aperio ScanScope system and the stained sections were evaluated by our pathologist using a brightfield microscope in a blinded fashion between the control and treatment groups for general tissue morphology, coherence of architecture and data analysis. The positivity of pRb-, p21-and Cleaved Caspase-3- stained cells was calculated as percentage over the total tumor cells, while the intensity score of LaminB1-, RRM2-and γH2AX stained cells was calculated according to the I*P formula: (maximum Intensity * cells Percentage) + (preponderant Intensity * cells Percentage). The IHC data are represented as a mean ± SD of two mice per each group.

RNA preparation and quantitative PCR analysis

Total RNA was extracted from cell pellet and tumor tissue samples using the Quick-RNA MiniPrep, following manufacturer's instructions. RNA was reverse transcribed into cDNA using OneScript Plus cDNA synthesis kit, following manufacturer's instructions. Real-time PCR analysis was performed on the Biorad CFX-96 instrument with 20ng of cDNA *per* reaction at 50°C for 2 min followed by an initial denaturation step at 95°C for 10 min, 40 cycles at 95°C for 30 s, 60°C for 30 s, and 72°C for 30s. The experiments were carried out in triplicate for each data point. The relative quantification of gene expression was determined using the $2^{-\Delta Ct}$ method. qPCR primers were designed for: USP7, CCNA2, CCNB1, CCND1, CCNE2, DNAJC9, UBE2V2, ELL2. Ribosomal Protein Lateral Stalk Subunit P0 (RPLP0) was used as a housekeeping gene.

Senescence-associated β galactosidase (SA-β-gal) activity

Seven days post-infection or 48 h post P5091 treatment, 4% paraformaldehyde-fixed cells were incubated in homemade SA-β-Gal staining solution at 37°C for 16h. Enzymatic reaction was stopped by washing the cells three times with ice-cold PBS and staining analyzed with EVOS microscope or inverted microscope. SA-β-Gal activity was also quantified by flow cytometry using Cellular Senescence Detection Kit - SPiDER-βGal as described in the manufacturer's protocols.

Senescence-associated secretory phenotype (SASP) analysis

Five days post-infection, MM27 and MM16 cells were seeded into six well plates at 100,000 cells/well. Conditioned media were harvested after 24h and stored at −80°C.

Milliplex antibody-specific beads were used to capture SASP-associated factors. The Luminex Discovery Assay was employed to analyze multiple SASP factors simultaneously, through capturing Milliplex antibody-specific beads. According to the manufacturer's instructions. Concentration of IL-1A, IL-1B, IL-6, IL-8, CCL2, CCL2, CXCL1, CXCL10, MMP3, ICAM1, TNFA and IFNG was measured by The Luminex 100/200 System.

Immunofluorescence staining

Five days post-infection, shScr and shUSP7 MM27 and MM16 cells were plated on glass coverslips. The following day, cells were fixed in 4% paraformaldehyde, permeabilized with 0.01% Triton X-, and blocked for 1 h with 2% BSA. The following antibodies were used: FITC-labeled p21, Cy3-labeled USP7, A555-coniugated Ki67. Slides were then counterstained with 4′,6-diamidino-2-phenylindole for nuclei labeling and mounted on glass slides with Mowiol. Images were collected at 40X and 63X magnification by motorized Leica DM6B fluorescence microscope, equipped with a Zyla camera, LASX Software. The immunofluorescent quantification analysis has been done with custom made ImageJ macro.

RNA-seq and mass spectrometry (MS)-based proteomic analysis

ShScr and shUSP7 MM27 and MM16 PDX cells were harvested 48h post-infection and triplicate cell pellets were collected and rinsed with PBS. Total RNA was extracted as indicated above and RNA-seq libraries were prepared from 1μg of total RNA using the TruSeq RNA Library Preparation Kit v2 according to manufacturer's instructions. The libraries were additionally purified using AMPure beads (Beckman Coulter), quality checked at Agilent 2100 Bioanalyzer and 50 bp paired-end sequenced on an HiSeq 2000 Sequencing System (Illumina). RNA-seq reads were aligned to genome (hg19, GRCh38) using TopHat2 2.0.9 (Kim et al., 2013) starting from 3×10^7 mapped paired-end reads per sample. Read counts of each gene were quantified using HTseq (Anders et al., 2015) and differential analysis was performed using DESeq bioconductor packages (Anders and Huber, 2010). Genes were identified as differentially expressed (DEGs) when the following criteria were met: $\log_2$fold-change (FC) $\geq |0.6|$, pAdj <0.01. DEGs were analyzed with Gene Ontology term enrichment using DAVID tool (version 6.8 Beta) (Huang et al., 2007), Ingenuity Pathway Analysis (IPA) and with GSEA (Gene Set Enrichment Analysis) software v2.2.0 (Subramanian et al., 2005). Gene sets enriched at FDR <0.25 were considered statistically significant.

For (MS)-based proteomic analysis, UPS7 KD and control MM25 and MM16 cell pellets were lysed in pre-heated SDS-containing buffer [10% SDS, 50% glycerol, 1 M tris-HCl (pH 7.4)], and sonicated. Protein lysates were centrifuged at maximum speed for 20 min. Protein extracts were quantified using the BCA Protein Assay Kit. Then, proteins were separated on NuPAGE Novex 4-12% gradient gels prior to MS analysis. In all cases, for each gel lane five consecutive bands were excised and protein were in gel trypsin-digested following previously described protocol (Shevchenko et al., 2006). In brief: proteins were reduced in 10 mM DTT for 1 h at 56°C and alkylated with 55 mM iodoacetamide for 45 min at room temperature in the dark. Digestion was carried out with 12.5 ng/μL trypsin overnight at 37°C. Tryptic peptides were extracted from the gel pieces with 3% trifluoroacetic acid (TFA) and 30% acetonitrile (ACN). The extracted peptides were concentrated using custom STAGE Tips microcolumns (Rappsilber et al., 2007). Peptides were then eluted in 40 μL buffer B (80% ACN, 0.1% formic acid (FA)). ACN was evaporated using a speed vac concentrator (Eppendorf) and the samples volumes were adjusted to 5 μL (1% TFA). Peptides were separated using an EASY-nLC 1200 (Thermo Fisher Scientific) coupled on line to a Q-Exactive HF mass spectrometer (Thermo Fisher Scientific) through a nano-electrospray ion source (EASY-SPRAY, Thermo Fisher Scientific). The nano-LC system was operated in one column set-up using a PEPMAP RSLC C18 column (2μm, 100 Å, 75 μm × 25 cm, Thermo Fisher Scientific) kept at 45°C constant. Solvent A was 0.1% formic acid (FA) and solvent B was 0.1% FA in 80% ACN. Samples were injected in aqueous solution 1% TFA at a constant pressure of 980 Bar. Peptides were separated with a gradient of 3–35% solvent B over 60 min followed by a gradient of 35–45% for 9 min and 45–65% over 5 min at a flow rate of 250 nL/min. The Q-Exactive was operated in data-dependent acquisition (DDA) to automatically switch between full scan MS and MSMS acquisition. MS spectra (from m/z 375-1650) were analyzed in the Orbitrap detector with resolution R = 60,000 at m/z 200. The 15 most intense peptide ions with charge states ≥ 2 were sequentially isolated to a target value of 3×10^6 and fragmented with a normalized collision energy (NCE) value of 28% in to the Higher-energy C-trap dissociation (HCD). The maximum allowed ion accumulation times were 20ms for full scans and 80ms for MSMS. The dynamic exclusion time was set to 20s. Acquired raw data were analyzed using MaxQuant software (version 1.6.2.3), using the integrated Andromeda search engine for protein identification (Tyanova et al., 2016). Both for MM27 and MM16 and dataset search parameters were the following: false discovery rate (FDR) both at proteins and peptides level was set to a maximum of 1%; carbamidomethylation of Cysteine was set as a fixed modification, whilst, Methionine oxidation and N-terminal acetylation were included as variable modifications. The UP000005640 (Uniport ID) database (78,120 Entries) was downloaded to be used for peptide identification and enzyme specificity was set to trypsin with two missed cleavages permitted. The MaxLFQ algorithm for label-free quantification was activated, as well as the match between runs (MBR) feature (matching time window = 0.7 min) (Cox et al., 2014). The ''protein groups'' output file from MaxQuant was analyzed using Perseus software (Tyanova et al., 2016). Briefly, no imputation was used, and the data were filtered to have 3 valid values in at least one group. Threshold setting for differential protein expression were S0 = 1, FDR = 0.01 for the comparison between UPS7 KD and control samples both in MM27 and MM16 derived dataset. Significant differentially expressed proteins (DEPs) with FDR 5% (pAdj<0.05) were indicated with a ''+'' in the corresponding column (see Table S3). Then, DEPs were analyzed as above reported for DEGs.

Protein–protein interaction networks functional enrichment analysis

The Search Tool for the Retrieval of Interacting Genes/Proteins database (STRING v11.0) was used to construct the Protien-Protein Interaction (PPI) network associated with USP7. The common 10 downregulated differential expressed proteins in MM27 and MM16 PDXs were submitted as a list of multiple proteins and were analyzed by String. The STRING database generates a network of PPI and these interactions are sourced from five main sources: Genomic Context Predictions, High-throughput Lab Experiments, (Conserved) Co-Expression, Automated Text mining and Previous Knowledge in Databases (Szklarczyk et al., 2017). The String analysis generated a PPI p value (2.25e-10) and functional enrichments in the identified network: we considered the UniProt Analysis.

Synchronization

PDX cells were treated with 2 mM thymidine overnight and then released from thymidine block by PBS wash, followed by the addition of complete medium. After 8 h, 2mM thymidine was added to the medium and cells cultured for additional 16 h. Cells were rinsed twice with PBS and released in complete growth medium for 0h (G1/S-phase cells), 4h (S-phase cells), 10h (G2/M-phase cells), 16h (G1-phase cells). Cells were collected and analyzed using flow cytometry and Western Blotting.

Protein stability assay

To detect protein half-life shScr and shUSP7 PDX cells were treated (1, 2, 4 h) with cycloheximide (CHX) two days post-infection. MG132 (10 μM) was added for 8h to inhibit proteasome activity. Crude extracts were prepared and protein levels were assessed by Western blot analysis.

Immunoprecipitation and western blot analysis

Cells were lysed in RIPA buffer (50 mM Tris-HCl pH 8.0, 150 mM Na-Cl, 1% NP-40, 0.5% sodium deoxycholate, 0.1% SDS, 50 mM) for western blotting (WB) and in JS buffer (50 mM HEPES pH 7.4, 150 mM NaCl, 10% glycerol, 0.5% NP40, 1.5 mM MgCl, 5 mM EGTA) for immunoprecipitation (IP). All buffers were supplemented with a protease and phosphatase inhibitor cocktail. For IP and co-IP assay, the buffer was also supplemented with 2mM of PMSF and with 25 μM UPS inhibitor, PR-619. Western blotting analysis was performed as previously described (Aladowicz et al., 2020). The following proteins were blotted: USP7, RRM2, p21, PARP-1, Lamin B1, P-(Ser807/811) Rb, p53, MDM2, P-(Ser2448) MTOR, P-(Ser139) H2AX, p16, Ub, p-(Thr229), p70 S6K, P-(Ser235/236) S6, ANLN, KIF11, HDAC2, HDAC3, Acetylated H3, H3. GAPDH and Vinculin were used as loading controls.

In vivo ubiquitination assay and Co-Immunoprecipitation

For the *in vivo* ubiquitination assay, shScr and shUSP7 MM27 PDX cells were treated for 8 h with 10 μM MG132 two days post-infection. Cells were then washed with PBS and lysed in RIPA buffer as indicated above. For S phase syncronization, cells were treated with 10 μM MG132 in the 4h of release following double thymidine block.

Protein concentration was quantified with the Bradford Assay. Cell lysates (~0.8 mg) were incubated 1h at 4°C in rotation with protein A Sepharose CL-4B beads and pre-cleared lysates were incubated with anti-RRM2 Antibody at 4°C for 3 h, followed by 1 h incubation with protein A beads in rotation. As negative control, cell lysates were immunoprecipitated with anti-IgG antibody. Immunocomplexes were washed with lysis buffer, boiled in SDS/PAGE sample buffer and analyzed by immunoblot analysis as above described. PVDF membranes were denatured in 6M Guanidium chloride, 50 mM Tris-HCl pH 7.5, 1mM PMSF, 5 mM β-mercaptoethanol for 30′ at 4°C for repeated blotting on the same membrane.

For the co-IP assay MM27 cells were infected with pLX304EV and pLX304 RRM2 vectors, and 9 h post-infection cells were synchronized as described above. Cell lysates (~1.5 mg) were immunoprecipitated and immunoblotted as reported above.

Proximity ligation assay (PLA)

In situ USP7-RRM2 interactions were detected by Proximity Ligation Assay kit, Duolink. Unsynchronized or S phase-synchronized MM27 cells were fixed and permeabilized as described above. Antibody incubation and probe amplification were performed according to the manufacturer's instructions. Cells were counterstained with DAPI for nuclei labeling. As negative controls, we performed the proximity ligation assay in the absence of primary antibodies. PLA spots were analyzed with custom-made ImageJ macro. Images were collected at 40X and 63X magnification by motorized Leica DM6B fluorescence microscope, equipped with a Zyla camera, LASX Software.

Rescue experiments

MM27 cells were co-infected with pLKO-shUSP7 and pLX304-RRM2 constructs or with empty vectors (pLKO-shScr and pLX304) or with single shUSP7 + pLX304 or with shSCR + pLX304. Cells were assayed after 120 h or 144h post-infection.

For the p21 silencing in shUSP7 depleted cells, MM27 cells were first infected with shUSP7 plasmid or pLKO-shScr as a control. Five days post-infection, cells were transduced with shp21 or pLKO-shScr as a control and after 5 days cells were assayed.

Tissue Microarrays (TMA)

Tissue Microarrays were performed in collaboration with the Division of Pathology and the Molecular Pathology Unit at the European Institute of Oncology (IEO), as already reported (Aladowicz et al., 2020). Human specimens derived from formalin fixed and paraffin embedded melanocytic lesions were arrayed as previously described (Luise et al., 2011).

USP7 expression levels were assessed by Immunohistochemistry (IHC) in the tumor tissue. Four-micron sections were cut, mounted on glass slides, deparaffinized, rehydrated, unmasked for 50 min in 0.25 mM ethylenediaminetetraacetic acid at 95°C and then treated for 5 min with 3% H_2O_2. Slides were then incubated overnight at +4°C with anti-USP7 antibody used at a dilution of 1:500 and revealed using the EnVision plus/horseradish peroxidase detection system (Dako) and counterstained with Hematoxilin. Slides were acquired with the Aperio ScanScope system (Leica Biosystems). USP7 expression was initially defined as low (IHC score 0.5–1), moderate (IHC score 1.5–2), or high (IHC score 3). Since only USP7 high expressing tumor shows the worst prognosis, we categorized tumor samples in high expression and low–moderate expression and presenting data as high vs. low protein expression. p-values (Pearson) were measured by chi-square test. TMA data analysis was performed using JMP 14.0 statistical software (SAS Institute, Inc).

IN VITRO DRUG TREATMENT

In vitro drug sensitivity and cytotoxicity was assessed by CyQuant and CellTox Green assay respectively in MM27 and MM16 cells. Briefly, for generating dose-response curves, the MM27 cells were plated in triplicate in 96 wells ($\sim 1.5\times10^3$/well) and treated by a single exposure to either the vehicle (DMSO) or increasing concentrations of P5091 (USP7 inhibitor) for 72 h. IC50 was calculated for P5091 (IC50 = 3.79 μM) using GraphPad Prism software. For the sequential combination treatment, MM27 and MM16 cells were seeded in triplicate in 96 wells ($\sim 0.9\times10^3$/well, $\sim 5.0\times10^3$/well respectively) and were treated with 5 μM P5091 or 5 μM FT671 or 7 μM GNE6640 for MM27, with 6 μM P5091or 8 μM FT671 or 12 μM GNE6640 for MM16 or DMSO. After 48h with a specific USP7 inhibitor, cells were sequentially treated for 72h with 0.35 μM domatinostat or 0.35 μM belinostat or 0.5 μM vorinostat for MM27, with 4 μM domatinostat or 2 μM belinostat or 5 μM vorinostat for MM16. The inhibition of viability is indicated over control, meanwhile the cell toxicity is indicated over the corresponding cell viability and over control (GraphPad Prism software).

QUANTIFICATION AND STATISTICAL ANALYSIS

Data are represented as mean ± SD of biological triplicates (if not, differently indicated in the text). Comparisons between two or more groups were assessed by using unpaired two-tailed Student's *t-test*.

For the statistical difference in tumor volume among different treatments, unpaired *t test* or one-way Anova *t test* were used. Log rank test and/or hazard ratio was used for survival analysis. Chi-square test was performed in TMA analysis.

For all the statistical tests: ns, not significant; *, $p < 0.05$; **, $p < 0.01$; ***, $p < 0.001$; ****, $p < 0.0001$.